Lawrence Berkeley National Laboratory

Title

Constraining Bedrock Groundwater Residence Times in a Mountain System With Environmental Tracer Observations and Bayesian Uncertainty Quantification

Permalink

https://escholarship.org/uc/item/0xd8r84x

Journal

Water Resources Research, 59(2)

ISSN

0043-1397

Authors

Thiros, Nicholas E
Siirila-Woodburn, Erica R
Dennedy-Frank, P James
et al.

Publication Date

2023-02-01

DOI

10.1029/2022wr033282

Copyright Information

Peer reviewed

Constraining Bedrock Groundwater Residence Times in a Mountain System With Environmental Tracer Observations and Bayesian Uncertainty Quantification

Nicholas E. Thiros[1] , **Erica R. Siirila-Woodburn[2]** , **P. James Dennedy-Frank[2]** , **Kenneth H. Williams[2,3]** , and **W. Payton Gardner[1]**

[1]Geosciences Department, University of Montana, Missoula, MT, USA, [2]Earth and Environmental Sciences Area, Lawrence Berkeley National Laboratory, Berkeley, CA, USA, [3]Rocky Mountain Biological Laboratory, Gothic, CO, USA

Abstract Groundwater residence time distributions provide fundamental insights on the hydrological processes within watersheds. Yet, observations that can constrain groundwater residence times over broad timescales remain scarce in mountain catchment studies. We use environmental tracers (CFC-12, SF_6, ^3H, and ^4He) to investigate groundwater residence times along a hillslope in the East River Watershed, Colorado, USA. We develop a Bayesian inference framework that applies a Markov-chain Monte Carlo (MCMC) approach to estimate noble gas recharge temperature, elevation, and excess-air parameters and the resulting environmental tracer concentrations. MCMC is then used to propagate the environmental tracer uncertainties to estimates of groundwater mean residence times inferred with lumped parameter models. All samples contain ^3H, CFC-12, and SF_6 in addition to terrigenic ^4He, suggesting a mixture of water characterized by modern and premodern residence times. ^4He exponential mean residence times range from hundreds of years at the upslope well to thousands of years at the toe-slope well assuming average crustal production rates. We find that binary mixing residence time distributions with separate young and old mixing fractions are needed to predict the ^4He, CFC-12, SF_6, and ^3H observations, supporting the importance of flow path mixing in this bedrock system. Our findings that the fractured bedrock hosts groundwater with a mixture of residence times ranging from decades to millennia suggest variable recharge dynamics and flow path mixing along the hillslope and highlight the importance of characterizing groundwater systems with observations that are sensitive to transport over a broad range of residence times.

Plain Language Summary Understanding how long water spends in mountain watersheds is critical to manage our water resources. In this work, we use natural chemical tracers measured in groundwater to improve understanding of groundwater flow and transport patterns and timescales. The technique we develop includes interpretation of dissolved noble gases to better constrain where in the watershed water (rain and snow) enters the groundwater system. We find that groundwater is preferentially generated at elevations higher than the groundwater wells. Our interpretation of the chemical tracers also suggests that the mountain groundwater has ages, or residence times, on the order of decades to thousands of years. This suggests that our water resources in this system potentially entered the groundwater aquifer at considerable times in the past. This work helps develop a further understanding of groundwater processes in mountainous systems, which is needed to improve our water resource predictions.

1. Introduction

Mountain groundwater systems store and transmit essential water resources and solutes locally within catchments and throughout the larger watershed (Frisbee et al., 2011; Hayashi, 2020; Viviroli et al., 2007). There is an increased recognition that groundwater in fractured bedrock can influence the overall hydrologic functioning in headwater catchments and is critical for processes such as stream baseflow (Engdahl & Maxwell, 2015; Tague & Grant, 2009), solute and contaminant exports to rivers (Carroll et al., 2018; Dwivedi et al., 2018), and plant transpiration dynamics (Fan et al., 2019; Harmon et al., 2020). While it is widely acknowledged that the subsurface hydrogeologic properties and land-surface processes (e.g., precipitation dynamics) exert primary controls on bedrock groundwater fluxes, these processes are spatially and temporally heterogeneous and remain uncertain within mountain systems (e.g., Appels et al., 2015; Carroll et al., 2019; W. P. Gardner et al., 2020; Markovich et al., 2016; Welch & Allen, 2014). Given the complexities in the mechanisms that dictate the parti-

Writing – original draft: W. Payton Gardner
Writing – review & editing: Erica R. Siirila-Woodburn, P. James Dennedy-Frank, Kenneth H. Williams, W. Payton Gardner

tioning of shallow soil water to bedrock groundwater recharge, there is a need to further develop integrated catchment hydrologic conceptual and numerical models constrained to in situ observations of bedrock groundwater dynamics. However, there is typically a paucity of observation data sets that can constrain bedrock groundwater processes in mountainous systems (e.g., Somers & McKenzie, 2020).

Groundwater residence time distributions (RTDs), or age distributions, provide a fundamental description of the groundwater flow and transport processes (Cook & Herczeg, 2000). Researchers have long used RTDs to help understand and quantify system processes that are difficult to directly observe, such as recharge rates (Cartwright et al., 2017; McCallum et al., 2017; Solomon & Sudicky, 1991), active circulation depths in mountain systems (Manning et al., 2021; Welch & Allen, 2014), flow path mixing (Maloszewski & Zuber, 1982; Marçais et al., 2022), and groundwater resource resilience to climate change (Singleton & Moran, 2010). Compared to interpretation of groundwater level observations alone, the information content provided by RTDs can be invaluable to alleviate the nonuniqueness in estimation of groundwater mass fluxes (McDonnell & Beven, 2014; Thiros et al., 2021). Groundwater RTDs, however, cannot be directly observed and are typically inferred from environmental tracer measurements (Cook & Herczeg, 2000; Sprenger et al., 2019). Mountain catchment studies often estimate RTDs using environmental tracers that can constrain short residence times (<5 years), for instance, using stable water isotopes sampled from streams (Benettin et al., 2022; McGuire & McDonnell, 2006; Sprenger et al., 2019). These observation data sets are insensitive to the groundwater flow and transport processes that occur over decadal and longer timescales (Suckow, 2014), resulting in a potentially incomplete and biased interpretation of the groundwater RTD and flow system (e.g., Frisbee et al., 2013). Improved characterization of bedrock groundwater RTDs over broader timescales is warranted as our conceptual and predictive models of mountain catchment hydrology continue to highlight and integrate flow through deeper bedrock reservoirs (Brooks et al., 2015; Condon et al., 2020; Singha & Navarre-Sitchler, 2021; Somers & McKenzie, 2020).

Environmental tracers with input signals that vary over decades (e.g., CFCs, SF_6, and ^3H) and noble gas radioisotopes that decay/accumulate with rates on the order of centuries to millennia (e.g., ^4He) have been useful to constrain groundwater RTDs over broad timescales (Suckow, 2014). Interpretation of long-residence time environmental tracers in mountain catchments suggests that bedrock groundwater RTDs can have components characteristic over timescales not identifiable using typical injection tracer tests nor stable water isotopes (Carroll et al., 2020; Gabrielli et al., 2018; Manning et al., 2021; Singleton & Moran, 2010). However, due to the inherent challenges with installing bedrock groundwater wells in mountain systems, applications of environmental tracers to constrain groundwater flow have largely focused on samples collected from streams (e.g., Carroll et al., 2020; W. P. Gardner et al., 2011), springs (e.g., Meyers et al., 2021), and valley aquifer wells (e.g., Manning & Solomon, 2003; Markovich et al., 2021). Mountain front recharge RTD dynamics estimated using samples from valley-bottom wells provide useful information over broad spatial scales, yet have limited ability to isolate processes at the subcatchment and hillslope scales. While samples collected from streams and springs can be used to characterize catchment RTDs at finer spatial resolutions, they integrate flow path and process heterogeneity from multiple subsurface compartments (e.g., soil, saprolite, and fractured bedrock), making it difficult to isolate the signal from bedrock groundwater alone (W. P. Gardner et al., 2020). Few studies have measured environmental tracers that are sensitive to long-residence time groundwater directly from bedrock wells in headwater mountain catchments (Gabrielli et al., 2018; Hale et al., 2016; Manning & Caine, 2007; Manning et al., 2021). Improved characterization of bedrock groundwater RTDs is needed to evaluate plausible mixing scenarios and hydrologic connectivity to the overlying shallow soil system. In this work, we add to the understanding of bedrock groundwater RTDs in high-elevation headwater catchments through interpretation of environmental tracers that can constrain residence times on the order of decades (CFCs, SF_6, and ^3H) and millennia (terrigenic ^4He) at the hillslope scale. While this environmental tracer set cannot inform the full distribution of plausible residence times (e.g., 1-year-old water), our analysis can provide insight on groundwater processes that are characteristic over a range of long timescales.

RTDs inferred from environmental tracers have numerous sources of uncertainty, both in the processing of field data and subsequent modeling. Two salient sources of uncertainties are assumptions regarding the RTD used in lumped parameter models (Maloszewski & Zuber, 1982; Massoudieh et al., 2012) and estimation of the sample recharge temperatures and excess-air conditions (e.g., Aeschbach-Hertig et al., 1999; Manning & Solomon, 2003). Complexities in RTDs are a function of the uncertain hydrogeologic property heterogeneity, variance in topography-driven flow paths, and spatially and temporally variable recharge (Suckow, 2014). While interpreting multiple environmental tracers can help constrain the unknown mixing processes (e.g., W. P. Gardner

et al., 2015; Massoudieh et al., 2012), the full RTD cannot be uniquely determined (McCallum et al., 2015) and must be assumed. Thus, understanding and quantifying the mixing processes that lead to observations of long-residence time bedrock groundwater in complex mountain systems that are sparsely observed remains a challenge. Popp et al. (2021) and Schilling et al. (2021) show the value of interpreting multiple environmental tracers that are sensitive to a range of residence times and groundwater processes to reduce uncertainty in mixing dynamic understanding.

Inference of RTDs in mountain systems is complicated by the a priori uncertain recharge temperatures, pressures, and excess-air conditions that are required to properly interpret gas-phase environmental tracers, such as CFCs, SF_6, and noble gas isotopes. While methods have successfully constrained these recharge parameters using noble gas measurements and prior information on the correlation between temperature and pressure (Doyle et al., 2015; Manning & Solomon, 2003; Markovich et al., 2021), groundwater RTD optimization procedures rarely propagate the inferred recharge uncertainties into environmental tracer concentration errors and subsequent mean residence time estimates. To our knowledge, interpretation of dissolved noble gas concentrations and recharge parameter uncertainties using a Bayesian framework that directly assimilates valuable prior knowledge on the covarying parameter distributions has not been performed. Thus, it is poorly understood how uncertainties in the noble gas recharge parameters propagate to RTD estimates and the evaluation of plausible mixing scenarios within mountain groundwater systems.

In this work, we investigate bedrock groundwater RTDs along a mountainous hillslope transect in the East River Watershed near Crested Butte, Colorado, using a suite of environmental tracer observations that can inform transport characteristics over decadal and millennia timescales. As a preliminary step in estimating groundwater mean residence times, we extend previous noble gas recharge parameter calibration methods (e.g., Jung & Aeschbach, 2018; Kipfer et al., 2002) to apply a Bayesian Markov-chain Monte Carlo (MCMC) procedure to infer joint posterior distributions (uncertainties) for recharge temperatures, elevations, and excess-air conditions. Our noble gas recharge parameter inference methodology differs from previous works in that it formally and jointly considers both prior information for all parameters and analytical measurement uncertainties for the dissolved noble gas observations. We then propagate the noble gas recharge and excess-air parameter uncertainties into field observations of environmental tracers CFC-12, SF_6, ^3H, and terrigenic ^4He. Groundwater mean residence times conditioned to the uncertain noble gas recharge parameters are interpreted using lumped parameter models assuming multiple commonly applied RTDs and a MCMC uncertainty quantification technique. While the proposed technique does not comprehensively account for all of the uncertain assumptions needed evaluate dissolved noble gases and mean residence times in mountain systems, we seek to develop a flexible framework to improve estimation of bedrock groundwater RTD uncertainties. These tools will allow improved investigation of groundwater processes within mountain aquifer systems around the world, as well as illustrate the source and role of long-residence time groundwater in mountain aquifers.

2. Study Area

The East River Watershed is within the Elk Mountains near Crested Butte, Colorado (Figure 1). The East River hosts a multidisciplinary watershed research site through the U.S. Department of Energy's and Lawrence Berkeley National Laboratory's Watershed Function Scientific Focus Area (Hubbard et al., 2018). This study is focused on groundwater samples collected from the northeast facing "Pumphouse" lower montane (PLM) hillslope within the East River Watershed (Figure 1). The PLM hillslope is ~1 km long, ranges in elevation from 2,650 to 2,930 meters above sea-level (m asl), and terminates at the floodplain of the East River. The climate is characterized as continental subarctic with mean daily temperatures recorded at the nearby Butte SNOTEL station ranging between −8.3°C in winter to 11°C in summer. The annual average precipitation is ~700 mm and occurs mostly as winter snowfall (~70%) from October through May and summer monsoon rains from July to September (Carroll et al., 2018). Land cover is characterized by grasses and shrubs and snow cover can persist through May. The East River hydrograph shows strong correlation with snowmelt patterns, with peak discharge typically in early June and baseflow conditions from October to April. Previous work at the PLM hillslope suggests that the bedrock groundwater recharge is dominated by snowmelt and contribution from summer monsoons is not expected due to high evapotranspiration rates (Tokunaga et al., 2019). While the PLM hillslope is within a montane ecosystem, catchment areas above the hillslope can reach 3,400 m asl and consists of subalpine and alpine ecosystems characterized by aspen and conifer vegetation, exposed barren and rock talus land cover, and colder temperatures with larger snowpacks that experience melt later in the year.
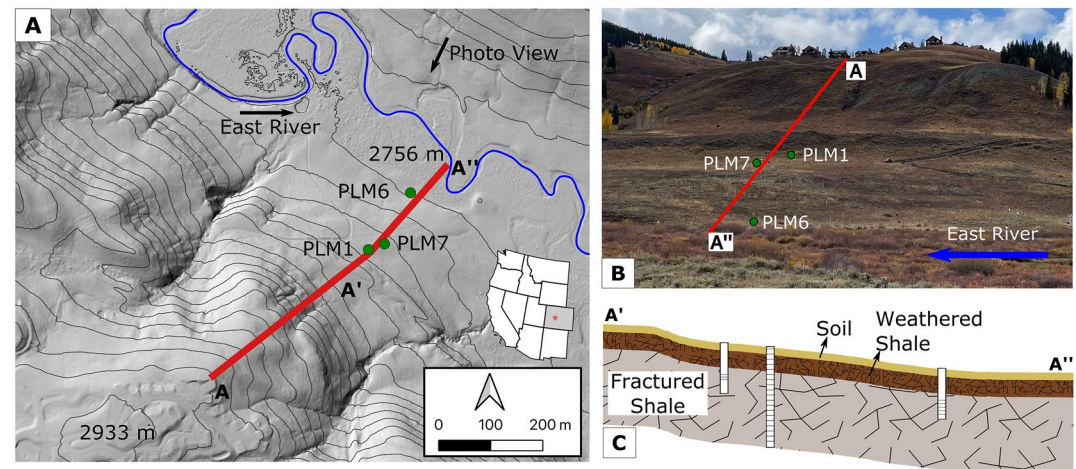
Figure 1. (a) Elevation contour map and (b) image of the study site located in East River Watershed near Crested Butte, Colorado. The red line indicates the Pumphouse lower montane (PLM) hillslope transect and the green dots are the locations of the three observation wells. (c) Simplified cross section along the bottom portion of the PLM hillslope transect showing well positions and screened intervals.

2.1. Hydrogeology

A simplified subsurface conceptual model of the PLM hillslope consists of shallow soil, weathered bedrock (saprolite), and fractured bedrock layers (Figure 1c; Tokunaga et al., 2019). At the PLM hillslope and surrounding lower basin areas, the bedrock lithology is a marine-derived Cretaceous Mancos Shale. Higher elevation regions of the basin that include Snodgrass Mountain and Mount Crested Butte additionally contain igneous intrusive quartz monzonite and granodiorite bedrock. The Mancos Shale bedrock at the PLM hillslope has experienced significant postdepositional increases in permeability due to alteration from mountain uplift events, alpine glaciation and deglaciation, extensional stress, and weathering processes (Miltenberger et al., 2021). Geologic descriptions of cores drilled up to 70 m below land surface (bls) indicate that the fractured bedrock starts at ~4 m bls. Fracture density is observed to decrease with depth, yet persists to at least 70 m bls at the drilling locations. However, comparison of cores from two deep boreholes that are ~200 m apart shows that fracture characteristics and bedrock hydraulic properties can vary significantly in space, likely due to local fault features (Miltenberger et al., 2021). Estimates of mean saturated hydraulic conductivity in the shallow fractured bedrock (<10 m bls) are 1.6×10^{-7} m s^{-1} (Tokunaga et al., 2019). Overlying the fractured bedrock is a ~1–3 m thick layer of highly weathered shale bedrock and ~1 m thick soil horizon. The soil textures are characterized as loam to silt loam with saturated hydraulic conductivity of 8.8×10^{-6} m s^{-1} (Tokunaga et al., 2019). Measured groundwater levels along the lower part of the hillslope fluctuate between 1 and 4 m bls, which generally corresponds to the thickness of a weathered bedrock zone (Wan et al., 2021).

3. Methods

3.1. Well Description and Environmental Tracer Sampling

An overview of the methodical workflow that includes interpretation of noble gases and residence time environmental tracers is shown in Figure 2. We sampled a suite of environmental tracers that includes dissolved noble gases (He, Ne, Ar, Kr, and Xe), chlorofluorocarbons (CFCs), sulfur hexafluoride (SF$_6$), and tritium (^{3}H) from three groundwater wells that are finished within the fractured shale bedrock on the PLM hillslope (Figure 1). The three wells (PLM1, PLM6, and PLM7) are located on the lower portion of the hillslope along a transect that spans a ~30 m elevation gradient that occurs over a horizontal distance of ~130 m. PLM1 is the most upslope well and is 10 m deep with screen between 6.3 and 7.2 m bls. PLM6 is at the toe of the hillslope near the floodplain and is 10 m deep with screen between 6.1 and 9.1 m bls. Further details on PLM1 and PLM6 can be found in Tokunaga et al. (2019). PLM7 is located between PLM1 and PLM6 and is 70 m deep with screen over the entire length. Water samples from PLM7 were collected at ~20 m bls (described below).
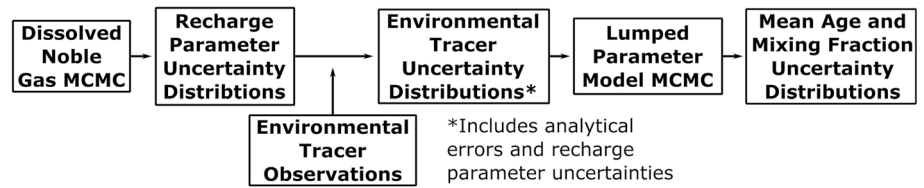
```
┌──────────┐   ┌──────────┐       ┌──────────┐   ┌──────────┐   ┌──────────┐
│Dissolved │   │ Recharge │       │Environ-  │   │ Lumped   │   │Mean Age  │
│  Noble   │──▶│Parameter │──────▶│mental    │──▶│Parameter │──▶│and Mixing│
│ Gas MCMC │   │Uncertainty│      │Tracer    │   │Model MCMC│   │Fraction  │
│          │   │Distribtions│     │Uncertainty│  │          │   │Uncertainty│
└──────────┘   └──────────┘       │Distributions*│ └──────────┘ │Distributions│
                     ▲             └──────────┘                  └──────────┘
               ┌──────────┐       *Includes analytical
               │Environ-  │        errors and recharge
               │mental    │        parameter uncertainties
               │Tracer    │
               │Observations│
               └──────────┘
```

Figure 2. Methodological workflow illustrating the primary steps performed to evaluate groundwater recharge parameters from dissolved noble gases and subsequent mean residence times from environmental tracers.

Groundwater samples from PLM1, PLM6, and PLM7 were collected between 5 May and 7 May 2021 using methods described by the University of Utah Dissolved Noble Gas Lab (http://www.noblegaslab.utah.edu). The shale bedrock experiences methane production and release (Wan et al., 2021), which can lead to groundwater degassing during sampling and complications with interpreting environmental tracers (Plummer et al., 2006). To limit the impact of potential degassing, we sampled all environmental tracers with down-hole pumps and back-pressure valves for the collection of noble gases (Aeschbach-Hertig & Solomon, 2013). Well PLM1 and PLM7 qualitatively did not show evidence of gas bubble formation during sampling, while PLM6 contained minor amounts. Dissolved noble gases were collected using the standard copper tube method (Aeschbach-Hertig & Solomon, 2013). CFCs were collected in triplicate in 250 mL glass bottles with no headspace. SF_6 was collected in duplicate in 1 L glass bottles with no headspace. ^3H was collected in duplicate in 500 mL plastic bottles. Samples at well PLM1 and PLM6 were collected after purging three borehole volumes and monitoring of steady field parameters. Due to the long well screen at PLM7, samples were collected at low-flow pumping rates to prevent water table draw down and after measured field parameters were stable. All environmental tracer samples were analyzed at the University of Utah Noble Gas Laboratory (http://www.noblegaslab.utah.edu).

3.2. Dissolved Noble Gases

3.2.1. Solubility Equilibrium and Excess Air

Dissolved noble gases (Ne, Ar, Kr, and Xe) have long been recognized as valuable tracers to constrain groundwater recharge temperatures (Aeschbach-Hertig et al., 1999; Kipfer et al., 2002). Noble gases dissolved into groundwater are chemically inert and have no appreciable internal sources within aquifers (with the exception of He). Concentrations in groundwater are controlled by the solubility equilibrium established at the groundwater table, which is given by Henry's law and is a function of the recharge temperature and total pressure (assuming negligible salinity; Kipfer et al., 2002). We use elevation Z in m asl as a proxy for the total pressure P (Pa) using the empirical lapse rate (Cook & Herczeg, 2000):

$$P = \left(1 - \frac{0.0065 \cdot Z}{288.15}\right)^{5.2561}. \tag{1}$$

It is common that measured noble gas concentrations in groundwater exceed solubility equilibrium concentrations (C^{eq}) at plausible recharge temperatures and elevations. This "excess-air" formation process has been attributed to the entrapment and subsequent dissolution of air bubbles during recharge (Heaton & Vogel, 1981). We model noble gas concentrations in groundwater as a function of solubility equilibrium and excess-air dynamics using the commonly applied closed-equilibrium (CE) model (Aeschbach-Hertig et al., 1999):

$$C_i^{atm}(T_r, Z, A_e, F) = C_i^{eq}(T_r, Z) + \frac{(1 - F) \cdot A_e z_i}{1 + F A_e z_i \cdot C_i^{eq}(T_r, Z)^{-1}}, \tag{2}$$

where C_i^{atm} (cm³STP/g) is the aqueous concentration of noble gas i = [He, Ne, Ar, Kr, and Xe] derived from atmospheric sources, T_r is the recharge temperature (°C), Z (m) is the recharge elevation, A_e (cm³STP/g) is the initial volume of entrapped excess air per unit volume of porous media, and F is a dimensionless excess-air fractionation parameter that describes the change in volume of the excess air in the final state compared to initial state at the water table during recharge. The CE model was chosen over other excess-air models because it can capture degassing processes (Aeschbach-Hertig et al., 2008). Equation 2 is additionally used to convert the measured CFCs and SF_6 aqueous concentrations to atmospheric mixing ratios that can be compared to historic time series (Section 3.3.1).

Table 1
Prior Distributions for the Noble Gas MCMC Parameter Inferences

Parameter	Low	High	Distribution
A_e (cm³STP/g)	10^{-4}	10^{-1}	$Beta(\alpha = 2, \beta = 2)$
F (−)	10^{-3}	10	$Beta(\alpha = 2, \beta = 2)$
Z (m)	2,786[a], 2,782[b], 2,759[c]	3,300	$Beta(\alpha = 2, \beta = 4)$
b (m)	2,889	3,719	$Beta(\alpha = 2, \beta = 2.5)$
	μ	σ	
m (m/°C)	−146	17	$Normal(\mu, \sigma)$

Note. The *Beta* distributions are scaled between the Low and High values using Equation 5.
[a]PLM1. [b]PLM7. [c]PLM6.

3.2.2. Noble Gas Recharge Parameters in Mountain Systems

Inference of T_r, Z, A_e, and F (hereinafter referred to as noble gas recharge parameters) is performed with parameter calibration techniques that compare modeled concentrations (Equation 2) against observed concentrations of the noble gases Ne, Ar, Kr, and Xe. He is excluded due to in situ subsurface production that is not considered in Equation 2 and is a function of the unknown groundwater RTD. Joint estimation of the four noble gas recharge parameters is ill posed when both T_r and Z are considered uncertain, as is the case in mountain systems that have large variations in topography. To constrain this parameter nonuniqueness using plausible process knowledge, studies have incorporated approximations of the recharge temperature-elevation lapse rate into the parameter calibration procedure (Doyle et al., 2015; P. M. Gardner & Heilweil, 2014; Manning & Solomon, 2003; Markovich et al., 2021). In particular, the best fit joint solution for T_r and Z is taken as the intersection of the assumed recharge lapse rate and a line that approximates all plausible solutions of Equation 2 constrained to noble gas measurements (see Manning & Solomon, 2003 for details). This calibration procedure can include uncertainties in the prescribed lapse rate (P. M. Gardner & Heilweil, 2014; Manning & Solomon, 2003) and least squares solutions of Equation 2 as the result of noble gas analytical measurement error (Jung & Aeschbach, 2018; Markovich et al., 2021). These previous applications of recharge parameter inference from noble gases observations, however, do not directly consider prior knowledge on all uncertain parameters. It is often the case that solutions to noble gas inversions vary from expectations and prior information on the parameters is applied in an ad hoc and subjective manner. We propose a Bayesian framework for the parameter inference problem that systematically and coherently assimilates prior knowledge on all recharge parameters (including the uncertain temperature lapse rate) to characterize the noble gas recharge parameter joint uncertainties.

3.2.3. MCMC Parameter Inference

Parameter inference using Bayesian methods quantifies the posterior distributions of uncertain model parameters **m** conditional on observation data $\mathbf{d}^{obs}$ and the prior parameter probability distributions $P(\mathbf{m})$ (Linde et al., 2017). The parameter posterior probability distributions $P(\mathbf{m}|\mathbf{d}^{obs})$ are quantified using Bayes' theorem:

$$P\left(\mathbf{m}|\mathbf{d}^{obs}\right) \propto P\left(\mathbf{d}^{obs}|\mathbf{m}\right)P(\mathbf{m}), \tag{3}$$

where $P(\mathbf{d}^{obs}|\mathbf{m})$ is the likelihood of the observations given a set of parameters. Our observation data are the vector of measured noble gas concentrations $\mathbf{d}^{obs} = $ [Ne, Ar, Xe, and Kr] within a sample from a single well. The posterior distributions in Equation 3 represent our updated estimate of the parameter uncertainties after considering both observation data and prior knowledge on parameter uncertainties. Similar to previous studies, our goal is to infer the joint posterior probability distributions for the noble gas recharge parameters described in Equation 2, while also taking into account an uncertain lapse rate. The lapse rate we consider is a linear equation that relates recharge elevations Z (m) to temperatures T (°C) as a function of an uncertain slope m (m/°C) and intercept b (m):

$$T = (Z - b)/m. \tag{4}$$

Thus, our parameter vector used within Equation 3 is $\mathbf{m} = [Z, m, b, A_e, \text{and } F]$ and recharge temperature posteriors are calculated using Equation 4.

Prior distributions are estimates of parameter uncertainties before the observation data are assimilated into the inference problem. Priors for Z, b, A_e, and F are considered *Beta* distributions scaled between a lower parameter bound b_l and upper bound b_u (Table 1) with the equation:

$$\frac{\mathbf{m} - b_l}{b_u - b_l} \sim Beta(\alpha, \beta). \tag{5}$$

Beta distribution priors were chosen due to the higher probability density on values in the center of the distribution, they are broad enough to allow a range of plausible values, and they provide discrete bounds on the physically based parameters (Brinkerhoff et al., 2021). The parameter bounds for A_e and F used in Equation 5 are
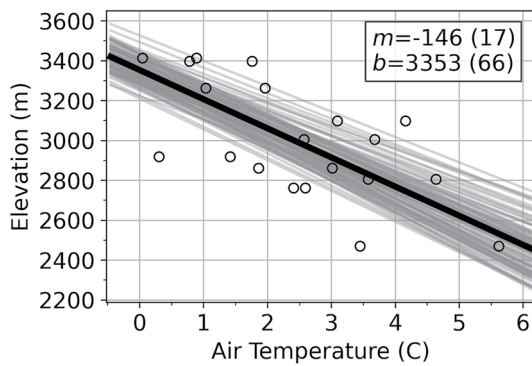
Figure 3. Annual average air temperature versus elevation measured at weather stations and STOTEL sites within the East River Watershed for the years 2019 and 2020. The thick black line corresponds to the mean linear lapse rate and the gray lines are random realizations from the slope (m) and intercept (b) posterior distributions. Values in parentheses are 1 standard deviation in the best fit parameters.

estimated from the literature and are meant to span a large range of plausible excess-air conditions. The a priori minimum and maximum possible Z are set as the elevation of the well and the top of the nearby Snodgrass Mountain, respectively. The recharge lapse rate priors were inferred by fitting a linear equation to annual average air temperatures recorded at 10 different weather stations and SNOTEL sites that range from ~2,460 to ~3,410 m elevation and are within the East River Watershed (Figure 3). Previous studies show the recharge lapse rates in mountain systems can have lower temperatures compared to the annual average air temperatures due to snowpack dynamics (Manning & Solomon, 2003; Masbruch et al., 2012). To account for this offset, the *Beta* prior for b is skewed such that there is approximately equal initial probability for the best fit atmospheric lapse rate ($b = 3,353$ m) and that which is depressed by 1°C ($b = 3,208$ m; Figure S1 in Supporting Information S1). The prior on the recharge lapse rate slope m is assumed normally distributed with a mean of -146 (m/°C) and 1 standard deviation of 17 m.

The likelihood function in Equation 3 quantifies the fit between model predictions (Equation 2) and observed dissolved noble gas concentrations. We use a Gaussian likelihood model in the form $P(\mathbf{d}^{obs}|\mathbf{m}) \sim N(\mathbf{d}^{obs}, \boldsymbol{\sigma}_{\mathbf{obs}})$, where $\boldsymbol{\sigma}_{\mathbf{obs}}$ is the observation analytical errors for the noble gases in $\mathbf{d}^{obs}$ (Visser et al., 2014). Gaussian likelihood models in this form make the common assumption that the errors between model predictions and observations are entirely characterized by the analytical uncertainties, thus do not account for epistemic uncertainties in the noble gas predictive model (Equation 2) nor observation data set. However, sole observation analytical observation error is likely not the case in our samples as we observe low Xe concentrations with respect to Ne, Ar, and Kr. This is consistent to the groundwater noble gas observations from Manning et al. (2021) in a nearby catchment with similar bedrock lithologies, who posit the low Xe can be caused by absorption to shale. Xe adsorption to shale bedrock has similarly been reported by Andrews et al. (1991). To account for added uncertainty not captured by Equation 2, we manually and subjectively increased the Xe uncertainty to 15% in $\boldsymbol{\sigma}_{\mathbf{obs}}$. This has the effect of lowering the influence that Xe has in the likelihood function and parameter estimation process.

The noble gas recharge and excess-air parameter posterior distributions (left-hand side of Equation 3) are inferred using a MCMC procedure (Gelman et al., 2014). The MCMC parameter inference uses the Adaptive Differential Evolution Metropolis algorithm (Ter Braak & Vrugt, 2008) implemented within the pyMC3 Python software. This MCMC sampler uses past states in each Markov-chain to inform future jumps, which improves the efficiency compared to the Metropolis-Hastings algorithm. We simulate four independent Markov-chains, each with 50,000 discrete samples from the posterior distribution. Both the Gelman-Rubin $\hat{R}$ statistic (Gelman et al., 2014) and visual examination of the Markov-chain traces were used to evaluate convergence of the posterior distributions, an adequate "burn-in" phase was established (set to 10,000 samples), and the entire parameter space was explored.

3.3. Groundwater Residence Time Distributions

3.3.1. Environmental Tracer Concentration Uncertainties

We estimate bedrock groundwater mean residence times and apparent ages using the environmental tracers CFC-12, SF$_6$, ^{3}H, and ^{4}He (Cook & Herczeg, 2000). Our interpretation of the CFC-12, SF$_6$, and ^{4}He observation uncertainties assimilates both the analytical observation errors and the noble gas recharge and excess-air posterior parameter distributions (Section 3.2). The observed CFC-12 and SF$_6$ aqueous concentrations are converted to an ensemble of atmospheric mixing ratios by evaluating the CE excess-air model (Equation 2) with the noble gas recharge parameter posterior distributions. The measured concentration of ^{4}He (^{4}He$_{obs}$) in a groundwater sample can be partitioned into components derived from atmospheric and terrigenic sources with the simplified mass balance equation (Cook & Herczeg, 2000):

$$^4He_{obs} = {}^4He_{atm}(T, E, A_e, F) + {}^4He_{ter}, \tag{6}$$

where ^{4}He$_{atm}$ is the combined concentrations due to solubility equilibrium and excess air (Equation 2). Terrigenic ^{4}He (^{4}He$_{ter}$) is produced during radioactive decay of uranium and thorium in aquifer grains, thus is the

component that is sensitive to groundwater residence times. Equation 6 does not account for He derived from mantle sources, which is a reasonable assumption for shallow wells in sedimentary bedrock systems. We estimate uncertainties in $^4\mathrm{He_{ter}}$ by propagating the noble gas recharge parameter posterior distributions to $^4\mathrm{He_{atm}}$ and considering the analytical uncertainties of $^4\mathrm{He_{obs}}$.

3.3.2. Groundwater Residence Time Models

Groundwater samples are characterized by a distribution of residence times as a result of flow path and diffusion mixing processes (Bethke & Johnson, 2008). While RTDs are known for idealized aquifers, details on the mixing processes remain uncertain in complex systems and are typically considered using lumped parameter models (e.g., Cook & Herczeg, 2000; Maloszewski & Zuber, 1982). Lumped parameter models describe the relationship between environmental tracer concentrations and RTDs using the convolution integral:

$$C_{out}(t) = \int_0^\infty C_{in}(t - t') g(t') e^{-\lambda t'} \, dt', \tag{7}$$

where $C(t)$ is the concentration at the sampling date t, t' represents residence times (years), $g(t')$ is the residence time distribution, $C(t - t')$ is the environmental tracer atmospheric concentration input function, and $e^{-\lambda t'}$ accounts for first-order decay reactions with decay rate λ ($\lambda^3_H = 0.056$ year^{-1}). The atmospheric input functions for CFC-12, SF_6, and ^3H are taken from the compiled data sets in Bullister (2017) and Michel et al. (2018). $^4\mathrm{He_{ter}}$ concentrations are assumed negligible in recharging water (i.e., for $t' = 0$).

We consider the dominant $^4\mathrm{He_{ter}}$ sources as in situ production and release from aquifer grains and crustal fluxes from external to the aquifer. $^4\mathrm{He_{ter}}$ accumulation rates J_{He} (cm^{3}STP/g/year) in groundwater are modeled as (Kipfer et al., 2002)

$$J_{He} = \Lambda_{He} \frac{\rho_r}{\rho_w} \left(C_U \cdot 1.19 \times 10^{-13} + C_{Th} \cdot 2.88 \times 10^{-14} \right) \cdot \left(\frac{1 - \theta}{\theta} \right), \tag{8}$$

where Λ_{He} is a release factor coefficient, ρ_r and ρ_w are densities of the rock and water, respectively, C_U and C_{Th} are the rock uranium and thorium concentrations (ug/g), respectively, and θ is porosity. Based on literature values representative of shale and analysis from a nearby site (Manning et al., 2021), rock properties are estimated as $C_U = 3.0$, $C_{Th} = 10.0$, and $\theta = 0.05$. Using the common assumption that ^{4}He is released into the groundwater at the same rate it is produced ($\Lambda_{He} = 1$), J_{He} is estimated as 3.3×10^{-11} $\left(\mathrm{cm^3 STP\, g_{H2O}^{-1}\, year^{-1}}\right)$ for all samples at the site. J_{He} varies between 2.4×10^{-11} and 4.2×10^{-11} $\left(\mathrm{cm^3 STP\, g_{H2O}^{-1}\, year^{-1}}\right)$ when evaluated with regional estimates of C_U and C_{Th} in Mancos Shale, which have 70% confidence intervals between 2 and 4 ppm and 8 and 12 ppm, respectively (Pliler & Adams, 1962). However, $^4\mathrm{He_{ter}}$ production rates typically remain highly uncertain due to unknown Λ_{He} (Solomon et al., 1996) and crustal He fluxes (Stute et al., 1992), which can both vary through space and time. Thus, J_{He} should be viewed as an approximation with a priori large uncertainties (Kipfer et al., 2002).

We test the ability of multiple, commonly applied parametric RTDs within Equation 7 to explain the observed environmental tracers and estimate plausible mean groundwater residence times τ (years). The RTD models are briefly described below (see Cook & Herczeg, 2000; Maloszewski & Zuber, 1982 for additional details). To follow convention in many groundwater studies, we use the terminology groundwater "age" synonymously with mean residence time. The piston-flow model (PFM) is the simplest RTD and assumes no mixing, thus all water in a sample is characterized by a single, scalar residence time. Due to these typically limiting assumptions, the piston-flow residence time is commonly referred to as an "apparent" groundwater age. The exponential model (EMM) RTD corresponds to complete mixing of a distribution of flow paths from zero-age to infinite-age waters. The EMM is fully characterized by the mean of the distribution, which approximates the mean residence time of the sample. The exponential piston-flow model (EPM) describes an aquifer with an exponential flow segment followed by a piston-flow segment. In addition to the mean residence time, the EPM has an additional shape parameter η, which can have the effect of excluding zero-age water from the RTD. Binary mixing models apply a weighted combination of two RTDs characterized by independent parameters. Here, we use a binary mixing model with a younger fraction described by an EPM and an older fraction described by a PFM (notated as EPM–PFM). The relative contribution of the EPM to the entire sample is given by f_1, while that of the PFM is $f_2 = 1 - f_1$. The EPM–PFM can represent, for instance, the conceptual model where premodern (recharged prior to ~1950 and does not contain CFC, SF_6, nor ^3H) groundwater from the deeper subsurface mixes into a shallow aquifer that is characterized by an EPM RTD.

Table 2
Prior Distributions for the RTD MCMC Analysis

Parameter	Low	High	Distribution
τ_1 (years)	1	1,000	*Uniform(Low, High)*
η_1 (−)	1	5	*Uniform(Low, High)*
f_1 (−)	0.01	0.99	*Uniform(Low, High)*
τ_2 (years)	50	15,000	*Uniform(Low, High)*
$t_{1/2}^{CFC12}$ (years)	5	35	*Beta($\alpha = 2, \beta = 2$)*
	μ	σ	
J_{He}[a] (cm³STP/g)	−10.48	0.33	*Normal(μ, σ)*
PE_{SF_6} (−)	0.0	0.167	*Half-Normal(μ, σ)*

Note. The *Beta* distribution is scaled between the Low and High values using Equation 5.

[a]Parameter is given as the $\log_{10}$ transform.

Additional sources of uncertainty that influence environmental tracer observations and residence time predictions include CFC degradation and SF_6 contamination (Cook & Herczeg, 2000; Plummer et al., 2006). All three wells had measurable dissolved oxygen, which suggests that anaerobic microbial degradation of CFC-12 is not likely. However, the shale bedrock contains methane as the result of methanogenesis, which has been shown to cause degradation of CFC-12 (Plummer et al., 2006). Following Massoudieh et al. (2012), we consider CFC-12 degradation in Equation 7 as a first-order decay process with an uncertain decay half-life. While SF_6 contamination due to point industrial sources is not expected due to the remoteness of the study site, contamination can occur from in situ production within sedimentary aquifers (von Rohden et al., 2010). We consider possible SF_6 contamination in Equation 7 as an uncertain percent increase relative to the observed SF_6 concentration (described below).

3.3.3. Groundwater RTD Inference

The RTD model parameters and associated uncertainties are inferred using a MCMC procedure similar to that presented for the noble gas analysis (Section 3.2.3). The prior distributi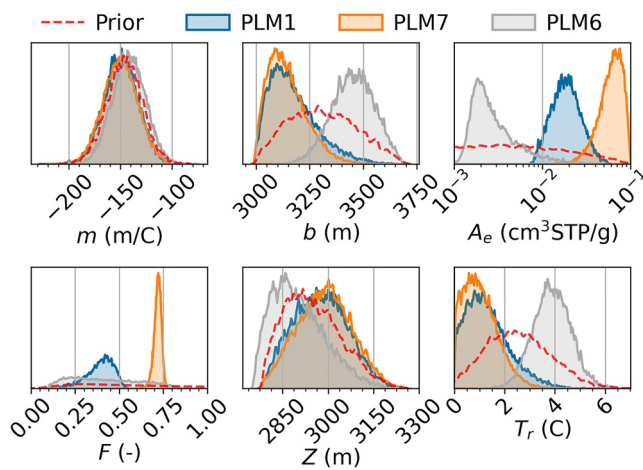ons for the uncertain RTD parameters are given in Table 2. In general, we apply uniform prior distributions with broad ranges for the model parameters τ, η, and f_1 due to sparse a priori knowledge on bedrock groundwater residence times in headwater catchments. Based on Equation 8 (and discussion therein), we assume the prior for J_{He} is log-normally distributed with mean −10.48 and a standard deviation of 0.33. This J_{He} variance generally matches uncertainty ranges reported in P. M. Gardner and Heilweil (2014), which was performed in the intermountain western United States in a predominately carbonate bedrock system. Despite the differences in the system studied here, the prior J_{He} distribution that constrains estimates within 1 order of magnitude of the mean can account for uncertainties due to a wide range of rock U and Th concentrations, He release factor coefficients, and crustal fluxes. The prior for the SF_6 contamination parameter $\left(PE_{SF_6}\right)$ is considered a half-normal distribution with a mean of zero and standard deviation of 0.17. This prior assumes that no SF_6 contamination is the most likely state and there is 99% probability (3σ) that contamination is within a ∼50% increase of the measured concentration. The prior for the CFC-12 degradation decay half-life $\left(t_{1/2}^{CFC12}\right)$ is considered a *Beta* distribution scaled between a lower parameter bound $b_l = 5$ years and upper bound $b_u = 35$ years with Equation 5. The $t_{1/2}^{CFC12}$ prior bounds are approximated from data presented in Hinsby et al. (2007). The η_1 prior ranges from 1 to 5, which corresponds to the EPM approaching exponential and piston-flow end-member shapes, respectively.

Given the relatively uninformative priors, the RTD parameter posterior distributions are predominantly controlled by the fit between predictions made by the lumped parameter model (Equation 7) and the environmental tracer concentrations. The environmental tracer concentrations are represented as uncertain distributions $\mathbf{C}_{ens}$ that assimilate both measurement analytical errors and the previously estimated noble gas recharge parameter uncertainties. The noble gas recharge parameters manifest in $\mathbf{C}_{ens}$ during the required conversion of the measured aqueous CFC-12 and SF_6 concentrations to atmospheric mixing ratios that can be compared to historical time series and in $^4He_{ter}$ during the component separations (further described in Section 3.3.1). The likelihood function assumes normally distributed model errors and is given by

$$P\left(\hat{\mathbf{C}}_{ens}|\mathbf{m}\right) \sim N\left(\hat{\mathbf{C}}_{ens}, \sigma_{\mathbf{C}_{ens}}\right),$$ (9)

where $\hat{\mathbf{C}}_{ens}$ is the mean of $\mathbf{C}_{ens}$, $\mathbf{m}$ are the uncertain RTD parameters, and $\sigma_{\mathbf{C}_{ens}}$ is standard deviation of $\mathbf{C}_{ens}$. For ^3H, $\sigma_{\mathbf{C}_{ens}}$ contains only the analytical uncertainty and $\hat{\mathbf{C}}_{ens}$ is the observation value without noble gas recharge parameter corrections. For the PFM and EMM RTD, we perform separate MCMC inferences using each of the environmental tracers alone to compare the variance in mean residence times estimates. We do not vary the model parameters that describe SF_6 contamination, CFC-12 degradation, and uncertainty in $^4He_{ter}$ production rates when considering each environmental tracer separately to avoid an ill-posed parameter inference problem. All of the environmental tracers (CFC-12, SF_6, ^3H, $^4He_{ter}$) are jointly considered to infer parameters for the EPM and

Figure 4. Noble gas recharge parameter prior distributions (red-dashed line) and posterior marginal distributions for wells PLM1 (blue), PLM7 (orange), and PLM6 (gray).

EPM–PFM RTD. Furthermore, variability in SF_6 contamination, CFC-12 degradation, and $^4He_{ter}$ production rates are incorporated for the EPM and EPM–PFM RTD parameter inferences.

4. Results

4.1. Noble Gas Recharge Parameters

The noble gas recharge parameter MCMC analysis converged for all parameters based on a qualitative assessment of four independent Markov-chain traces adequately exploring the parameter space and producing Gelman-Rubin $\hat{R}$ measures less than 1.05. Figure 4 shows the marginal posterior distributions for the noble gas recharge temperature (T_r) and elevation (Z), atmospheric lapse rate slope (m) and intercept (b), and excess-air parameters (A_e and F) at the three observation wells. The posterior distributions are considered to be within reasonable ranges for a high-elevation montane site and are consistent with studies in nearby basins (Carroll et al., 2020; Manning et al., 2021). We consider reductions in parameter posterior uncertainties relative to the prior distributions as a measure of parameter sensitivity to the observation data set and modeling structure.

The maximum a posteriori (MAP) corresponds to the parameter value with the highest probability and is the most likely given the analysis. The posterior Z distributions are similar for PLM1 and PLM7, with MAP estimates of ~3,000 m and standard deviations of ~100 m (Figure 4). Z at PLM6 is lower with a MAP estimate of 2,860 m and standard deviation of ~88 m. The posterior distributions for m show minimal changes compared to the prior distributions. Thus, m has little influence on the simulated noble gas concentrations given the modeling framework. The b posterior distributions are skewed to lower elevations at PLM1 and PLM7 (MAPs of ~3,100 m) relative to the prior of b = 3,353 m (Figure 3). At PLM6, the estimated b of 3,430 m is greater than the most likely prior values. T_r shows similar patterns to b. At wells PLM1 and PLM7, T_r is approximately 0.8°C with standard deviations of less than 1.0°C. T_r at PLM6 is warmer, with a MAP estimate of 3.7°C and standard deviation of 0.7°C. The excess-air parameters F and A_e show the largest uncertainty reductions relative to the priors. The most likely F estimates range from 0.42 to 0.72 with standard deviations less than 0.1 at wells PLM1 and PLM7 and 0.2 at well PLM6. The MAP A_e ranges from 0.002 cm³STP g⁻¹ at PLM6 to 0.063 cm³STP g⁻¹ at PLM7 with uncertainties on the order of 50% of the MAP values. ΔNe, which is a measure for total excess air, ranges from 68% at PLM1 to 16% at the PLM6 (Table S3 in Supporting Information S1).

Figure 5 illustrates the joint posterior distributions for recharge elevations and temperatures, along with simulations of the lapse rates sampled from the posterior distribution. The most likely recharge elevations at PLM1 and PLM7 are generally 200 m above the well heads (horizontal dashed lines), which are near or above the top of the hillslope transect (Figure 1). The recharge elevation for PLM6 is focused in the ~50 to ~100 m above the well and
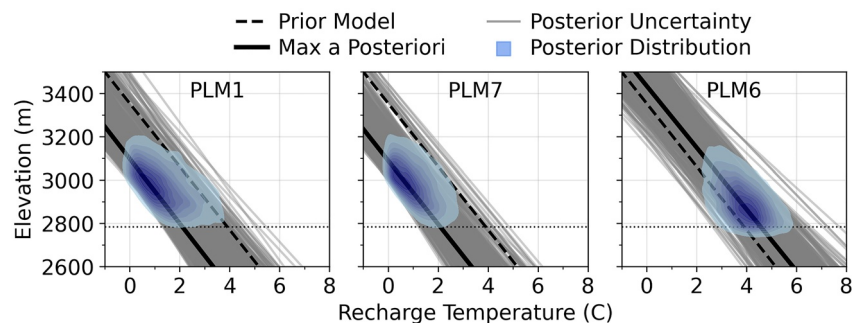

Figure 5. Simulated recharge temperature versus elevation posterior distributions (shaded blue), lapse rates from the joint posterior distributions (gray lines), the maximum a posteriori parameter estimate (solid black line), and the prior (dashed black line). Darker blue indicates higher probability density of recharge temperature and elevation. The horizontal dotted line is the well elevation.
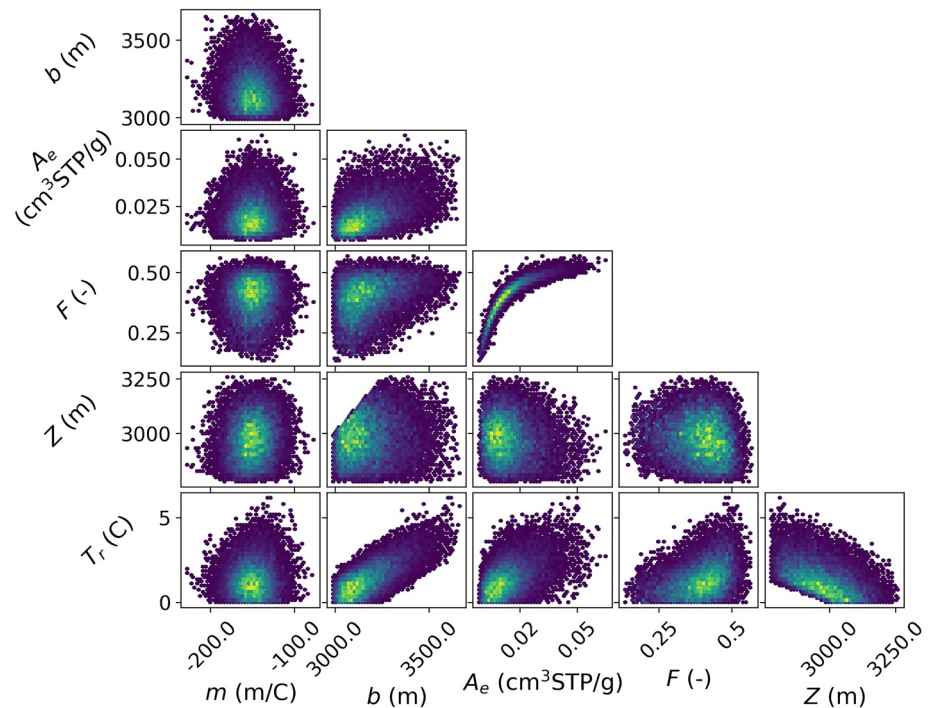
Figure 6. Noble gas recharge parameter joint posterior distributions assuming the closed-equilibrium (CE) model at well PLM1. Yellow and purple regions correspond to the highest and lowest posterior probabilities, respectively.

does not predict significant recharge from the higher elevation regions. For wells PLM1 and PLM7, the influence of depressing the lapse rate intercept b relative to the prior lowers the recharge temperature for a given elevation. At the toe-slope PLM6 well, the lapse rate falls to the right of the prior model (Figure 5), suggesting that recharge temperatures are warmer than the predicted annual average air temperature.

The MCMC inference methodology considers all parameter sets that are consistent with observations and prior information, and robustly quantifies the covariation between the parameters. The noble gas recharge parameter joint posterior distributions for well PLM1 are shown in Figure 6. Wells PLM6 and PLM7 show similar parameter correlation structures and are presented in Figures S2 and S3 in Supporting Information S1. Linear correlations exist between T_r, Z, and b due to the deterministic, yet uncertain, lapse rate used to relate these variables (Equation 4). The excess-air A_e and F parameters additionally show positive correlations with T_r, which is similar to the analysis in Jung and Aeschbach (2018). The correlation structure between A_e and F is positive and skewed such that increases of A_e beyond ~0.02 cm³STP g⁻¹ do not result in commensurate increases in F. We note that inferring the uncertainty of the non-Gaussian joint distribution of A_e and F is problematic for typical nonlinear least squares inversion techniques (Tarantola, 2005).

Figure 7 compares the observed noble gas concentrations and analytical errors (dashed-gray curves; Table S1 in Supporting Information S1) with the posterior predictive concentration distributions (filled-blue curves). At all three wells, there is good agreement between the observed and simulated Ne and Ar concentrations, with biases below the observation analytical uncertainties. The simulated Xe agrees with field observations at PLM1 and PLM7; however is overpredicted at PLM6. This bias is likely due to Xe sorption to the shale bedrock, which has been previously reported in the nearby Redwell Basin (Manning et al., 2021) and the Milk River Aquifer in Canada (Andrews et al., 1991). The simulated Kr concentrations underpredict the observations at wells PLM1 and PLM7. Improved Kr model fits require parameter values outside the prior distributions. In particular, increasing the simulated Kr concentrations at wells PLM1 and PLM7 requires recharge temperatures below 0°C, which are physically implausible.
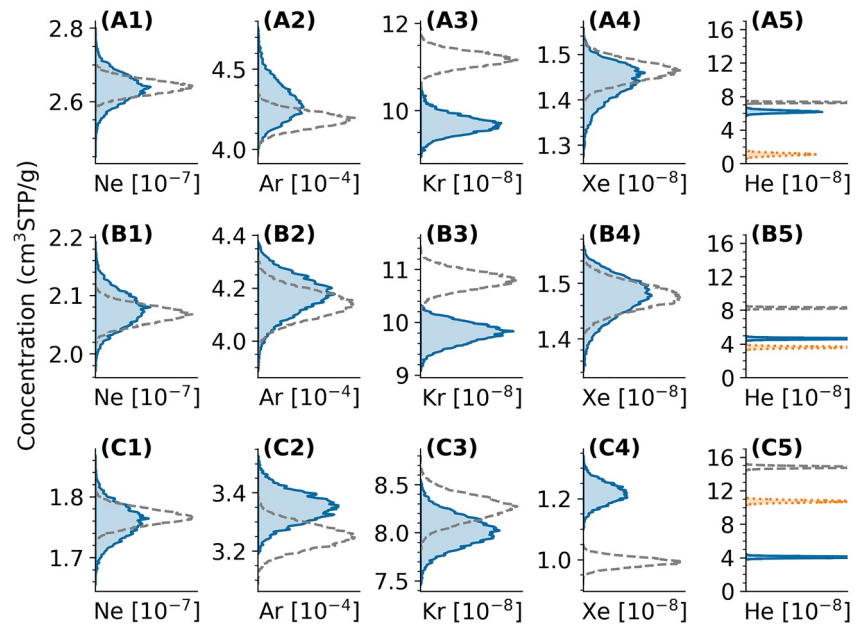
Figure 7. Posterior predictive noble gas concentrations at (a) PLM1, (b) PLM7, and (c) PLM6. The blue curves show the simulated posterior predictive noble gas concentrations (after Markov-chain Monte Carlo [MCMC] inference conditioned to Ne, Ar, Xe, and Kr) and the gray dashed-curves show the field observations. For He, the orange dotted-curve is the estimated terrigenic He component, calculated as the difference between observed and simulated He concentrations.

4.2. Groundwater Residence Times

4.2.1. Apparent Ages and Exponential Mean Residence Times

The CFC-12 observation distributions that account for the noble gas recharge conditions range from ~12 pptv at PLM6 and PLM7 to ~36 pptv at PLM1, with uncertainties of ~5% (Table 3). The CFC-12 apparent ages are 60, 68, and 68 years at PLM1, PLM7, and PLM6, respectively, which are near the piston-flow age dating limit for CFC-12. Figure 8 shows the posterior distributions of the exponential RTD model mean residence times for each of the environmental tracers. The low CFC-12 concentrations result in MAP exponential mean residence times of 615, 1,935, and 1,927 years at PLM1, PLM7, and PLM6, respectively. We note that in addition to the CFC-12 concentrations approaching preindustrial background concentrations, CFC-113 was not observed above analytical detection limits and only PLM1 had detectable CFC-11. While these CFC patterns can suggest large fractions of premodern groundwater (defined as recharge prior to the year 1950), similar patterns can been attributed to CFC degradation (Hinsby et al., 2007; Plummer et al., 2006). SF_6 apparent ages are 37 and 49 years and MAP exponential mean residence times are 146 and 702 at PLM1 and PLM7, respectively (Figure 8). The SF_6 concentration of 17 pptv at PLM6 is above plausible solubility equilibrium and excess-air conditions, suggesting the sample is contaminated. Possible sources of contamination include field sampling and terrigenic SF_6 production, which has previously been observed in sedimentary geologic settings (von Rohden et al., 2010). ^3H

Table 3
Posterior Predictive Concentrations

Well	$^4He_{ter}$ (cm^{3}STP/g)	±	Δ^4He_{ter} (%)	±	CFC-12 (pptv)	±	SF_6 (pptv)	±	^3H (TU)	±
PLM1	1.08e−8	2.13e−9	17	4	36.54	2.25	1.28	0.07	4.87	0.39
PLM7	3.60e−8	1.83e−9	77	5	11.92	0.69	0.29	0.02	4.32	0.35
PLM6	1.07e−7	3.09e−9	262	10	11.95	0.73	17.24	0.97	4.16	0.33

Note. $^4He_{ter}$, ΔHe_{ter}, CFC-12, and SF_6 assimilate observation analytical errors and noble recharge parameter uncertainties, while ^3H only assimilates observation analytical errors. ± refers to 1 standard deviation errors.
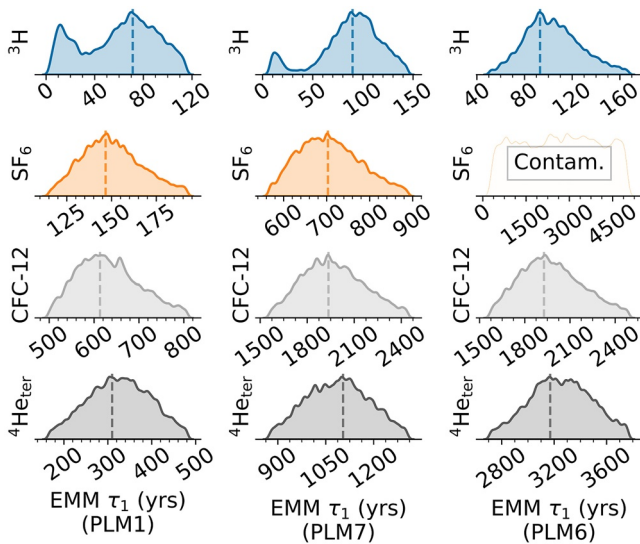
Figure 8. ^3H, SF_6, CFC-12, and $^4He_{ter}$ exponential residence time distribution (RTD) model (EMM) mean residence time posterior distributions at wells PLM1, PLM7, and PLM6. The $^4He_{ter}$ mean residence time estimates assume only in situ production at equilibrium diffusive conditions (see text for further details). Dashed vertical lines correspond to the maximum a posteriori (MAP) parameter estimate.

concentrations decrease from 4.9 TU at the upslope PLM1 well to 4.2 TU at the downslope PLM6 well. These ^3H concentrations result in nonunique apparent ages that can range from <10 years to ~60 years. The MAP ^3H exponential mean residence times are 71, 90, and 93 at PLM1, PLM7, and PLM6, respectively (Figure 8). Despite the variance and disagreement between the apparent ages and exponential mean residence times among the young environmental tracers, the presence of CFC-12, SF_6, and ^3H suggests that all the samples contain a component of modern groundwater.

Figure 7 indicates that all samples have ^4He in excess of predicted atmospheric equilibrium and excess-air sources, suggesting the presence of $^4He_{ter}$ and a fraction of long-residence time groundwater within the sample (Solomon et al., 1996). Δ^4He_{ter} is used to notate the $^4He_{ter}$ concentrations as a percentage of the combined atmospheric equilibrium and excess-air concentrations (C_{mod} in Figure 7). At wells PLM1, PLM7, and PLM6, Δ^4He_{ter} is 17%, 77%, and 262%, respectively (Table 3). Uncertainties in Δ^4He_{ter} are ~20% of the MAP value at PLM1 and less than ~5% of the MAP value at wells PLM7 and PLM6. $^4He_{ter}$ apparent ages and MAP exponential mean residence times are 310, 1,100, and 3,170 years at PLM1, PLM7, and PLM6, respectively (Figure 8), with the assumption that the He flux out of mineral grains equals in situ production (Equation 8).

4.2.2. RTD Prior Predictive Distributions

The cooccurrence of the young residence time environmental tracers (CFC-12, SF_6, and ^3H) and $^4He_{ter}$ suggests that the groundwater samples contain a mixture of residence times characterized by modern and premodern timescales. We qualitatively test the ability of multiple parametric RTDs to jointly explain the observed environmental tracers by randomly sampling from the RTD prior parameter distributions (Table 2) and comparing simulated concentrations from the lumped parameter model (Equation 7) against observations. Figure 9 shows the predicted concentrations for ^3H, SF_6, and CFC-12 versus $^4He_{ter}$ calculated using a constant production rate of 3.3×10^{-11} cm^{3}STP g$_{H2O}^{-1}$ year^{-1} (see Equation 8). The EMM and EPM RTD can approximate the joint SF_6 and $^4He_{ter}$, and CFC-12 and $^4He_{ter}$ observations. However, these RTD models cannot jointly explain the $^4He_{ter}$ and ^3H observations. In particular, simulations that contain $^3H > 4$ TU contain too little $^4He_{ter}$ compared to the field interpretations. The right column in Figure 9 suggests that the binary mixing EPM–EPM can better reconcile the young residence time environmental tracers with the inferred $^4He_{ter}$ concentrations. The uncertainties in the $^4He_{ter}$ production rate, CFC-12 degradation, and SF_6 contamination are not addressed in the prior predictive distribution plots, but are considered in subsequent MCMC parameter inferences.

4.2.3. RTD Model Parameter Inference

We quantitatively infer parameter uncertainties for the EPM RTD and EPM–PFM binary mixture RTD using MCMC analysis and the full set of environmental tracers (CFC-12, SF_6, ^3H, and $^4He_{ter}$). Furthermore, the EPM and EPM–PFM posterior distributions consider uncertainties in the $^4He_{ter}$ accumulation rates, CFC-12 degradation, and SF_6 contamination. The SF_6 observation at PLM6 was excluded from the parameter inference process due to contamination that is in excess of the prior models. Figure 10a shows the EPM mean residence time posterior distributions at wells PLM1, PLM7, and PLM6. The posterior distributions for the remaining uncertain parameters are presented in Figure S4 in Supporting Information S1. At PLM1, the MAP mean residence time (τ_1) is 82 years and the distribution ranges from approximately 60 to 130 years. PLM7 and PLM6 have older mean residence times of 122 and 140, respectively, and similar uncertainties that range from approximately 100 to 200 years. These results suggest that there is a 49% increase in the mean residence time moving downslope from PLM1 to PLM7 then a smaller 14% increase moving from PLM7 to the toe-slope well PLM6. The mean age increases by 2.1 years per meter change in land-surface elevation along the hillslope transect between upslope PLM1 well and toe-slope PLM6 well. Figure 10b compares the environmental tracer observations to the posterior predictive concentrations for the EPM. In general, the EPM predicts all the environmental tracer observations with reasonable uncertainty intervals.
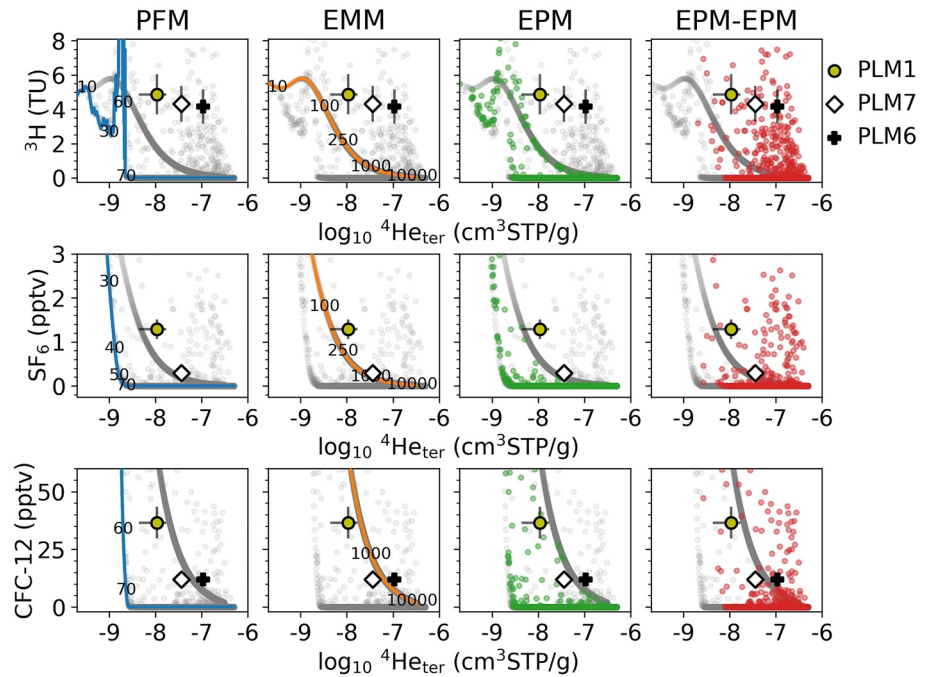
Figure 9. ^{3}H, SF$_6$, and CFC-12 versus ^{4}He$_{ter}$ bivariate tracer–tracer concentration plots generated using 15,000 Monte Carlo samples for each residence time distribution (RTD) model. Each RTD model has its own color and the gray points are the full set of model runs. For the piston-flow model (PFM) and exponential model (EMM), all plausible concentrations fall along a line. Labeled numbers on the PFM and EMM correspond to apparent age and mean age, respectively.

Figure 11a shows the mean residence times and mixing fraction parameter posterior distributions for the EPM–PFM binary mixing. Here, the subscripts, 1 and 2, refer to the young mixing component that is characterized with a EPM and the old mixing component that is characterized with a PFM, respectively. The posterior distributions for the remaining uncertain parameters are presented in Figure S5 in Supporting Information S1. The mean residence time of the young mixing component (τ_1) at PLM1 is 40 years and makes up between 0.65 and 0.99 (f_1) of the total sample (Figure 11a). PLM7 and PLM6 have similar τ_1 posterior distributions that range from ~45 to 115 years, with higher probability at mean residence times less than 100 years. The f_1 posteriors at PLM7 and PLM6 have broad distributions, yet, they have zero probability density at values approaching unity. This suggests that PLM7 and PLM6 cannot be explained using the young EPM component alone and mixing with longer residence time groundwater is required. Similarly, none of the wells have probability density for f_1 approaching
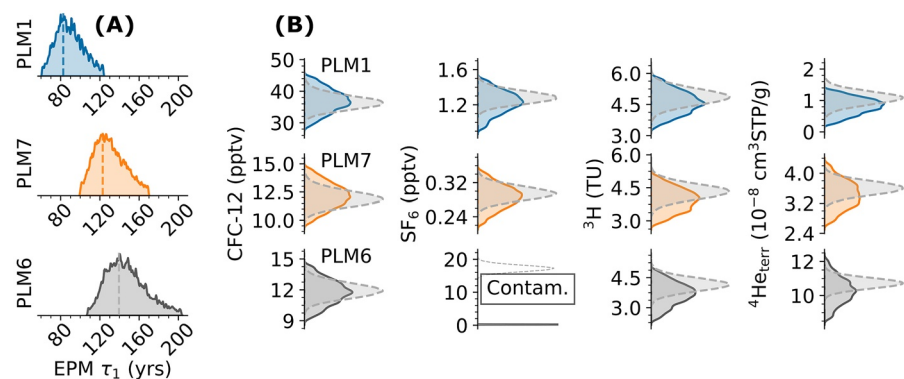

Figure 10. (a) Exponential piston-flow model (EPM) residence time distribution (RTD) mean residence time posterior distributions at wells PLM1, PLM7, and PLM6. (b) Posterior predictive concentrations (solid-filled curves) and observation distributions (dashed-filled gray curves) for the environmental tracers CFC-12, SF$_6$, ^{3}H, and ^{4}He$_{ter}$ used for the Markov-chain Monte Carlo (MCMC) inference.
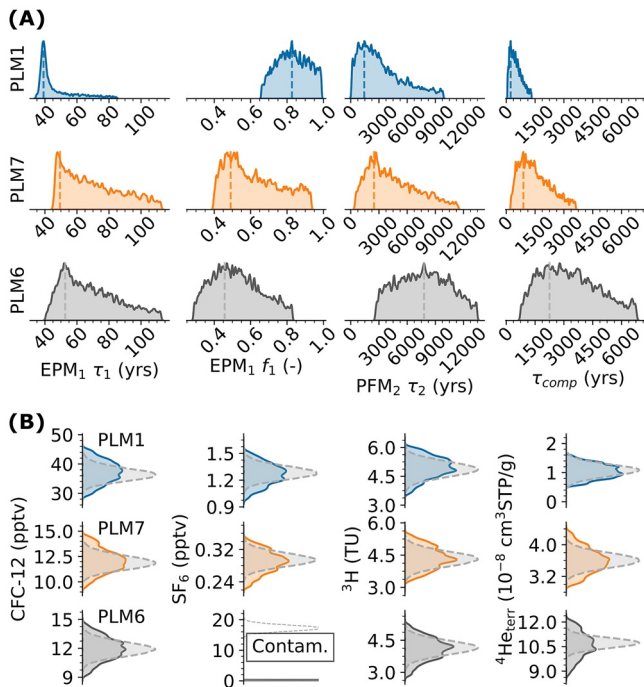
Figure 11. (a) Mean residence time posterior distributions at wells PLM1, PLM7, and PLM6 for the binary mixing model residence time distribution (RTD) that combines a young exponential piston-flow (EPM1) component with an old piston-flow (PFM2) component. (b) Posterior predictive concentrations (solid-filled) and observation distributions (dashed-gray curves) for the environmental tracers CFC-12, SF_6, ^3H, and $^4He_{ter}$ used for the Markov-chain Monte Carlo (MCMC) inference.
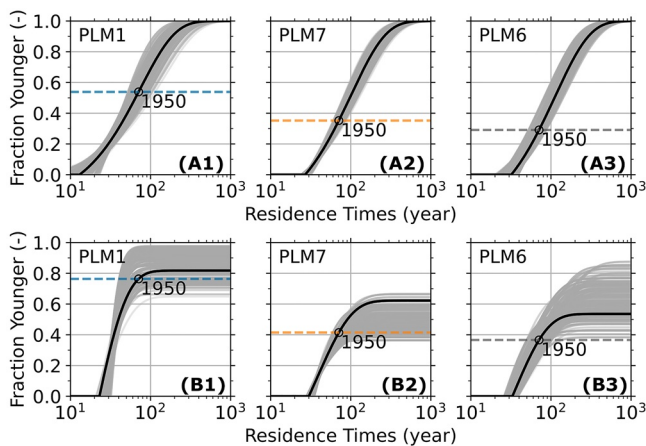

Figure 12. Groundwater residence time cumulative density distributions assuming (a) the exponential piston-flow model (EPM) residence time distribution (RTD) and (b) the binary mixing EPM–piston-flow model (PFM) RTD. The solid black curve is the average distribution of residence times and the light gray curves are samples from the posterior distribution. The open circle and corresponding horizontal line corresponds to the fraction of the total sample that is characterized with residence times that are modern (after 1950).

0.2 and less. This suggests a young component is needed to explain the environmental tracer suite. For all three wells, the mean residence time of the old PFM mixing component (τ_2) has broad posterior distributions with uncertainties on the order of thousands of years (Figure 11a). At PLM1 and PLM7, the τ_2 posterior distributions have ranges similar to the uniform prior distributions used in the MCMC analysis, but the more likely values are skewed toward younger mean residence times. Alternatively, the τ_2 posterior distribution at PLM6 has zero probability density below ~2,500 years and uniformly predicts mean residence times ranging from ~3,000 to ~10,000 years.

The EPM–PFM mean residence times that combine the young and old mixing fractions are notated as τ_{comp} in Figure 11a. Both the MAP estimates and variance of τ_{comp} increase moving downslope from PLM1 to PLM6. At wells PLM1 and PLM7, the τ_{comp} posterior distributions are skewed toward younger mean residence times and the most probable estimates are 227 and 892 years, respectively. At PLM6, the posterior τ_{comp} distribution does not have a well-defined maximum, but generally predicts mean residence times that are greater than 1,000 years. The increased fraction of long-residence time groundwater at PLM6 compared to PLM1 and PLM7 is consistent with the commensurate increase in $^4He_{ter}$ concentrations, but is also likely influenced by the lack of a SF_6 measurement that puts further constraints on the young mixing fraction. Figure 11b compares the environmental tracer field observations to the posterior predictive concentrations and suggests the EPM–PFM predicts all the environmental tracer observations with reasonable uncertainty intervals.

Figure 12 illustrates the cumulative density functions of both the EPM and young fraction of the EPM–PFM (the EPM component of the binary mixture model) evaluated with the respective posterior parameter distributions. These curves represent the entire RTD, rather than a probability distribution of the mean residence time. Figure 12 can be interpreted as the fraction of the total sample that is younger than a given residence time or, equivalently, recharged after a given date. For instance, regions of the curves that plot below the horizontal dashed lines indicate the proportion of the sample with residence times that are modern, which we define as recharged after the year 1950. RTD inference assuming the EPM suggests that 53% of the PLM1 sample is considered modern (Figure 12a1). At well PLM7 and PLM6, the percent of modern groundwater decreases to ~30% (Figures 12a2 and 12a3). The EPM–PFM RTD increases predictions of modern groundwater to 76%, 41%, and 36% of the total sample at PLM1, PLM7, and PLM6, respectively. Thus, the EPM–PFM predicts higher fluxes of modern groundwater compared to the EPM, despite τ_2 and τ_{comp} being on the order of hundreds to thousands of years (Figure 11).

5. Discussion

5.1. Noble Gas Recharge Zones

Understanding the temporal and spatial scales of bedrock groundwater flow and transport is critical for the further development of integrated hydrological conceptual models in headwater mountain catchments (Brooks et al., 2015; Condon et al., 2020). Interpretation of environmental tracers is one of the few methods available to constrain RTDs over timescales commensurate with the range of expected flow paths in mountain systems with steep topography and strongly contrasting hydrogeologic properties (e.g., Engdahl & Maxwell, 2015; W. P. Gardner et al., 2020). However, estimation of bedrock

groundwater RTDs using in situ measurements of environmental tracers has been limited and typically remains uncertain. This uncertainty is in-part due to the challenges with interpreting dissolved noble gases and inference of groundwater recharge conditions in mountain systems.

Studies have typically inferred variations in dissolved noble gas recharge parameters in mountain systems at the catchment to watershed spatial scales using deep production wells in the lower elevation valley (P. M. Gardner & Heilweil, 2014; Manning & Solomon, 2003; Markovich et al., 2019). While the inferred groundwater recharge elevations and temperatures have been valuable to constrain predictions of mountain block recharge locations (e.g., Doyle et al., 2015), expected variations in dissolved noble gases along smaller mountain hillslopes remain relatively unknown (Manning et al., 2021; Masbruch et al., 2012; Singleton & Moran, 2010). Our results suggest that bedrock wells spaced within 200 m of each other along the bottom half of a steep mountain hillslope have variations in inferred noble gas recharge temperatures, elevations, and excess-air conditions (Figure 4).

At the further upslope wells PLM1 and PLM7, the predicted recharge elevations are near or above the top of hillslope and have cold recharge temperatures approaching 0°C. High recharge elevations persist, even when considering the full uncertainty distributions of the joint parameters (Figures 5a and 5b), which accounts for the plausibility of colder ground and soil temperatures compared to mean air annual temperatures (Manning & Solomon, 2003; Masbruch et al., 2012). This implies that it is unlikely that the near 0°C recharge temperatures are solely sourced from low elevation recharge near the wells that consists entirely of cold snowmelt. The plausibility of recharge at elevations higher than the hillslope transect can suggest limitations in the hillslope 2D cross-section conceptual model (e.g., Figure 1c) that does not capture intermediate and regional flow paths from nearby mountain regions.

Compared to PLM1 and PLM7, the predicted recharge elevations are lower and temperatures are higher at the toe-slope well PLM6 (Figure 5). The increased recharge temperature can be the result of enhanced mixing with shallow alluvial water recharged locally on the lower elevation regions of the hillslope. This is consistent with the topography-driven flow path conceptual model where the base of hillslopes captures a broader distribution of flow paths, including very short flow paths (Engdahl & Maxwell, 2015). Numerical modeling by W. P. Gardner et al (2020) provides further process insights that support varying degrees of bedrock and shallow soil water mixing at toe-slope versus further upslope positions. In particular, they show that lower hillslope positions experience longer duration of hydraulic connectivity compared to upslope positions where bedrock recharge largely occurs during brief periods of high soil saturation conditions. This conceptual model is also consistent with the observation of a thinner and less transient unsaturated zone at PLM6, compared to the upslope wells (Tokunaga et al., 2019).

An alternative explanation for the higher recharge temperatures at PLM6 is an increased contribution of deep flow paths that reestablish equilibrium conditions with warmer, geothermally altered groundwater. These deeper flow path contributions are expected to have longer residence times (Frisbee et al., 2013; Gleeson & Manning, 2008), which is supported by the increased $^4He_{ter}$ concentrations moving downslope. Nonetheless, the toe-slope well shows distinct dissolved noble gas characteristics compared to further upslope wells, suggesting that there are variations in the distribution of groundwater flow paths along the lower section of the studied hillslope. This distribution of flow paths can integrate over spatial scales ranging from the local hillslope to the more distant higher elevation regions of the basin, which are rarely considered in conceptual models of hydraulic exchanges within hillslopes. Further characterization of the groundwater contributions sourced from higher elevation regions that may be buffered from snowpack changes can be critical to properly asses mountain catchment water balances in a drying climate (Carroll et al., 2019).

5.2. Variations in Mean Residence Times

There is an increased recognition that bedrock groundwater is an important component of mountain catchment hydrological functioning (e.g., Gabrielli et al., 2012; Singha & Navarre-Sitchler, 2021). Characterization of bedrock groundwater RTDs provides a first-order approximation on subsurface flow path dynamics (Asano & Uchida, 2012; Hale et al., 2016), which are generally difficult to observe and directly characterize in mountainous systems. Groundwater residence times are often reported as piston-flow apparent ages or mean residence times estimated from a single environmental tracer data point.

An important consideration in our analysis is that there are disagreements in apparent age and exponential model mean residence time inferred when using the different environmental tracers. Variations in tracer-specific

groundwater mean residence times has been previously discussed (e.g., Zuber et al., 2005) and has been attributed to processes such as microbial degradation of CFCs, contamination of SF_6, and incorrect RTD model assumptions (Cook & Herczeg, 2000; W. P. Gardner et al., 2011; Hinsby et al., 2007). In particular, groundwater mean residence times inferred from CFCs, SF_6, and ^3H observations can be biased when the sample contains a mixture of residence times that are not accurately captured in the assumed RTD (McCallum et al., 2015). These are known as aggregation errors and can lead to groundwater apparent ages that underpredict the true mean residence times of groundwater mixtures (Bethke & Johnson, 2008; Stewart et al., 2017). Aggregation errors can vary for different environmental tracers, resulting in groundwater age estimates that do not agree (W. P. Gardner et al., 2015).

Both aggregation errors and potential SF_6 contamination result in apparent groundwater ages biased toward younger values. Our inferred SF_6 apparent ages of 37 and 48 years at wells PLM6 and PLM7, respectively, are expected to provide estimates of minimum mean residence times for the bedrock groundwater samples given the tracer suite and presented techniques. These apparent ages are similar to mean residence times inferred using environmental tracers in other mountain catchments (Gabrielli et al., 2018; Hale et al., 2016; Manning et al., 2012; Singleton & Moran, 2010), which are older compared to residence times inferred using stable isotopes alone (e.g., McGuire & McDonnell, 2006). However, apparent groundwater ages that assume piston-flow conditions are expected to poorly represent the mixing processes in complex mountain groundwater systems, thus likely underestimate the true, but unknown, mean residences times. The presence of a considerable amount of premodern water mixed with modern water found in this study suggests that mountain groundwater residence times reported in previous studies can be missing long-residence time fractions and potentially biased young. Matrix diffusion is an alternative conceptual model to help explain the considerable premodern fractions (Cook et al., 2005; Rajaram, 2021). Diffusive exchange of environmental tracers between immobile matrix pore water and actively flowing fracture water can lead to estimated mean ages that are greater than the true mean age of the mobile water. Further work is needed to test these conceptual models in efforts to improve our understanding of bedrock groundwater RTDs in mountain watersheds.

The bedrock groundwater samples show evidence of mixing between groundwater characterized by modern and premodern residence times. This is qualitatively based on the cooccurrence of environmental tracers first introduced into hydrologic systems in the ~1950s (CFC-12, SF_6, and ^3H) and elevated $^4He_{ter}$, which is suggestive of residence times on the order of centuries to millennia (Solomon et al., 1996). Our results further support that interpreting mean residence times with RTD models that allow for mixing processes lead to older mean age estimates compared to the apparent ages. We find that introducing groundwater with premodern residence times into the sample mixture improves the ability to explain the full suite of environmental tracer observations. With an assumed EPM RTD, the most likely bedrock groundwater mean residence times along the hillslope are on the order of 80–140 years (Figure 10). The EPM RTD, which has been previously used to infer groundwater mean residence times in mountain catchments (e.g., Gabrielli et al., 2018), is a smooth function that is characterized by a single mean residence time. Alternatively, studies often observe that RTDs that consider a binary mixture of groundwater characterized by disparate young and old residence time fractions best fit multiple environmental tracers in mountain systems (W. P. Gardner et al., 2011; Lerback et al., 2022; Manning et al., 2012; Markovich et al., 2021). Our results similarly find that the EPM–PFM RTD can explain the observation data by mixing in a long-residence time fraction that is ~1 order of magnitude older than the young fraction (Figure 11). However, even when we consider mixing of an old water source, the mean residence time of the young fraction still contains a significant proportion of water with residence times of 50 years (Figure 12b). In our system, analysis of multiple environmental tracers interpreted using multiple RTD conceptual models suggests that the shallow bedrock wells have mean groundwater residence times on the order of 50–150 years, with a significant component of premodern water.

Few studies have quantified groundwater residence times in mountain catchments with environmental tracers that can inform mixing fractions with residence times characteristic on the millennia timescales (Frisbee et al., 2013; Manning & Caine, 2007; Manning et al., 2021). It is plausible that our interpretation of hillslope bedrock groundwater mean residence times that are older than values often reported in the literature is due to the assimilation of ^4He, which decreases the degree of residence time information truncation (Frisbee et al., 2013; W. P. Gardner et al., 2015). This idea was similarly presented in Hale et al. (2016) who identified evidence for bedrock groundwater samples that contain a mixture of modern and premodern residence times. However, they infer $^3H/^3He$ piston-flow apparent ages, which are relatively insensitive to mixing fractions characterized by premodern residence times. Another possible factor contributing to the older mean residence times reported in

this study is that the sampled wells are located lower in the mountain watershed network (lower stream order) compared to many prior studies that are in first-order stream catchments. Lower watershed elevation regions can include longer flow paths with larger residence times (Frisbee et al., 2011). Compared to this work, Manning et al. (2021) report similar elevated $^4He_{ter}$ values in bedrock wells from a nearby basin within the East River Watershed, further supporting our results that shallow subsurface systems in mountain headwater systems can be characterized with significant premodern residence time components. The observation of very old water, when using tracers capable of identifying old water, highlights the need to use multiple environmental tracers that can inform groundwater transport over broad timescales.

Our results show an increase in mean residence times moving downslope from well PLM1 to PLM6. This pattern is consistent with a topography controlled groundwater flow system where higher proportions of flow paths with long-residence times discharge to the lower hillslope positions (Gabrielli et al., 2018; Gleeson & Manning, 2008; Hale et al., 2016; Manning et al., 2012). Our analysis of the EPM–PFM RTD suggests that the increase in mean residence time at well PLM6 is largely the result of the old-fraction mixing component, which is most sensitive to the $^4He_{ter}$ observations. The presence of a young mixing fraction within all the samples is consistent with the conceptual model of a bedrock groundwater system that is hydraulically connected with modern recharge conditions and the overlying shallow subsurface system. This supports studies that suggest active circulation depths in mountain systems can extend deeper than the soil and saprolite regions and into bedrock (Carroll et al., 2020; Condon et al., 2020; W. P. Gardner et al., 2020; Tokunaga et al., 2019). The observed hydraulic connectivity between the soil and bedrock suggests that hillslope numerical models should be designed to capture the exchanges between these reservoirs over broad timescales (e.g., Rapp et al., 2020).

Given well PLM6 is at the toe of the slope in a groundwater discharge zone, we hypothesize that groundwater with residence times on the order of centuries to millennia are contributing to the shallow subsurface saprolite and soil groundwater systems. Upwelling of bedrock groundwater to high-conductivity zones at the bottom of the hillslope has been simulated numerically (W. P. Gardner et al., 2020). Groundwater discharge to these reservoirs has been shown to contribute to catchment evapotranspiration fluxes (e.g., Ryken et al., 2022) and streamflow generation processes (e.g., Hale et al., 2016). It has further been suggested that groundwater reservoirs characterized with premodern residence times can produce hydrologic and ecosystem resilience during drought conditions (Meyers et al., 2021; Singleton & Moran, 2010). Thus, it is critical to understand the processes that dictate the observed long-residence time fractions, and how inclusion of these flow paths changes predictions of integrated catchment hydrologic and ecological response to change.

5.3. Limitations

Modeling of dissolved noble gases has numerous sources of model structural errors that can influence the inferred recharge parameters. For instance, annual average air temperature lapse rates can poorly predict recharge temperatures in snow-dominated catchments (Manning & Solomon, 2003; Masbruch et al., 2012). Markovich et al. (2021) use numerical models to show that recharge lapse rates can deviate from linear relationships in systems with steep topography due to redistribution of water in the shallow subsurface prior to recharge events, which is also supported by model results from Carroll et al. (2019) and W. P. Gardner et al. (2020). Similarly, interpretation of dissolved noble gases in groundwater systems employs the piston-flow assumption, thus does not consider the impact of groundwater mixing with variable recharge conditions.

While our mean residence time estimates consider CFC-12 degradation, SF_6 contamination, and variation in $^4He_{ter}$ production rates, these processes remain uncertain and there exists little field data to directly constrain the associated parameters. The introduction of these parameters into the inference process without adequate data to constrain them results in higher uncertainties in the RTD parameter posterior distributions. Alternatively, there are numerous model structural errors and assumptions that were not considered uncertain in this work. For instance, ^3H concentrations in groundwater recharge are uncertain, yet they were assumed error free. Further work is needed to more comprehensively evaluate RTD uncertainties with environmental tracer observations.

The ^4He mass balance is typically not closed in shallow subsurface aquifers (Kipfer et al., 2002). In particular, it is difficult to distinguish between upwelling of deep groundwater flow paths (Stute et al., 1992) or elevated matrix diffusion processes (Solomon et al., 1996) using ^4He, as both can lead to elevated signals of long-residence time groundwater. This has implication for the provenience and flow path structure of the long-residence time

groundwater we observe. Further interpretation of RTDs that include diffusion processes that are salient in fractured bedrock systems (e.g., W. P. Gardner et al., 2016; Rajaram, 2021) and process-based numerical modeling frameworks that simulate groundwater flow and transport over broad spatial and temporal scales (e.g., Thiros et al., 2021) can be powerful tools to further interrogate the source and catchment function of the observed long-residence time fractions.

The environmental tracer suite used in this work cannot inform the full distribution of potential residence times. This includes residence times on the order of years to a decade and hundreds of years. For example, studies show the value of stable water isotopes and radon to constrain subdecadal residence times (Popp et al., 2021; Schilling et al., 2021; Sprenger et al., 2019) and ^{39}Ar to inform residence that are on the order of centuries (e.g., Visser et al., 2013). Interpreting more environmental tracers that inform diverse timescales (e.g., W. P. Gardner et al., 2015) and time series of environmental tracers (e.g., Visser et al., 2019) will likely further reduce groundwater RTD uncertainties.

6. Conclusions

Constraining bedrock groundwater flow dynamics and RTDs are fundamental challenges in mountain hydrology, yet necessary for refining conceptual models of mountainous water cycles. While gas-phase environmental tracer observations such as dissolved CFCs, SF_6, ^{3}H and nobles gases can provide invaluable insights on bedrock groundwater RTDs, there remains significant uncertainties due to nonuniqueness in noble gas recharge parameters. With the developed MCMC uncertainty quantification technique, we find that the noble gas recharge temperatures and elevations have large variability between three bedrock groundwater wells located within tens of meters of each other on the lower portion of a steep, mountainous hillslope. Based on MCMC uncertainty analyses with multiple commonly used RTD models, we show that the shallow bedrock on the studied hillslope is best described as a mixture between premodern and modern residence times. Terrigenic ^{4}He concentrations increase from the upslope to downslope wells, suggesting higher fluxes of groundwater characterized by premodern residence times. In addition to the markers of premodern residence times in the shallow bedrock wells, there simultaneously is evidence for a recently recharged fraction with modern residence times. The RTDs that include both premodern and modern mixing fractions suggest that the bedrock groundwater reservoir is connected to shallow soil hydraulic dynamics, which are more sensitive to contemporary recharge conditions and the effects of climate change. This work provides valuable insights on how mountain systems store and transmit essential water resources and highlights the need to further include bedrock groundwater processes in mountain catchment conceptual and integrated model predictions.

Data Availability Statement

The environmental tracer data from the Pumphouse Lower Montane groundwater wells in the East River Watershed and Python modeling scripts to interpret the data are available on the Zenodo repository at https://zenodo.org/record/7554795#.Y8qxti-B2uM (Thiros, 2023). Data and model are freely available and meet FAIR principles. The Python modeling scripts are actively developed on GitHub at https://github.com/nthiros/NobleGas_RTD_MCMC.

References

Aeschbach-Hertig, W., El-Gamal, H., Wieser, M., & Palcsu, L. (2008). Modeling excess air and degassing in groundwater by equilibrium partitioning with a gas phase. *Water Resources Research*, *44*, W08449. https://doi.org/10.1029/2007WR006454

Aeschbach-Hertig, W., Peeters, F., Beyerle, U., & Kipfer, R. (1999). Interpretation of dissolved atmospheric noble gases in natural waters. *Water Resources Research*, *35*(9), 2779–2792. https://doi.org/10.1029/1999WR900130

Aeschbach-Hertig, W., & Solomon, D. K. (2013). The noble gases as geochemical tracers. In P. Burnard (Ed.), *Advances in isotope geochemistry*. Springer. https://doi.org/10.1007/978-3-642-28836-4

Andrews, J. N., Drimmie, R. J., Loosli, H. H., & Hendry, M. J. (1991). Dissolved gases in the Milk River Aquifer, Alberta, Canada. *Applied Geochemistry*, *6*(4), 393–403. https://doi.org/10.1016/0883-2927(91)90039-R

Appels, W. M., Graham, C. B., Freer, J. E., & McDonnell, J. J. (2015). Factors affecting the spatial pattern of bedrock groundwater recharge at the hillslope scale. *Hydrological Processes*, *29*(21), 4594–4610. https://doi.org/10.1002/hyp.10481

Asano, Y., & Uchida, T. (2012). Flow path depth is the main controller of mean base flow transit times in a mountainous catchment. *Water Resources Research*, *48*, W03512. https://doi.org/10.1029/2011WR010906

Benettin, P., Rodriguez, N. B., Sprenger, M., Kim, M., Klaus, J., Harman, C. J., et al. (2022). Transit time estimation in catchments: Recent developments and future directions. *Water Resources Research*, *58*, e2022WR033096. https://doi.org/10.1029/2022WR033096

Bethke, C., & Johnson, T. (2008). Groundwater age and groundwater age dating. *Annual Review of Earth and Planetary Sciences*, *36*(1), 121–152. https://doi.org/10.1146/annurev.earth.36.031207.124210

Brinkerhoff, D., Aschwanden, A., & Fahnestock, M. (2021). Constraining subglacial processes from surface velocity observations using surrogate-based Bayesian inference. *Journal of Glaciology*, *67*(263), 1–19. https://doi.org/10.1017/jog.2020.112

Brooks, P. D., Chorover, J., Fan, Y., Godsey, S. E., Maxwell, R. M., McNamara, J. P., & Tague, C. (2015). Hydrological partitioning in the critical zone: Recent advances and opportunities for developing transferable understanding of water cycle dynamics. *Water Resources Research*, *51*, 6973–6987. https://doi.org/10.1002/2015WR017039

Bullister, J. L. (2017). Atmospheric histories (1765–2015) for CFC-11, CFC-12, CFC-113, CCl_4, SF_6 and N_2O (NCEI Accession 0164584). NOAA National Centers for Environmental Information. Unpublished Dataset (Tech. Rep.).

Carroll, R. W., Bearup, L. A., Brown, W., Dong, W., Bill, M., & Willlams, K. H. (2018). Factors controlling seasonal groundwater and solute flux from snow-dominated basins. *Hydrological Processes*, *32*(14), 2187–2202. https://doi.org/10.1002/hyp.13151

Carroll, R. W., Deems, J. S., Niswonger, R., Schumer, R., & Williams, K. H. (2019). The importance of interflow to groundwater recharge in a snowmelt-dominated headwater basin. *Geophysical Research Letters*, *46*, 5899–5908. https://doi.org/10.1029/2019GL082447

Carroll, R. W., Manning, A. H., Niswonger, R., Marchetti, D., & Williams, K. H. (2020). Baseflow age distributions and depth of active groundwater flow in a snow-dominated mountain headwater basin. *Water Resources Research*, *56*, e2020WR028161. https://doi.org/10.1029/2020WR028161

Cartwright, I., Cendón, D., Currell, M., & Meredith, K. (2017). A review of radioactive isotopes and other residence time tracers in understanding groundwater recharge: Possibilities, challenges, and limitations. *Journal of Hydrology*, *555*, 797–811. https://doi.org/10.1016/j.jhydrol.2017.10.053

Condon, L. E., Markovich, K. H., Kelleher, C. A., McDonnell, J. J., Ferguson, G., & McIntosh, J. C. (2020). Where is the bottom of a watershed? *Water Resources Research*, *56*, e2019WR026010. https://doi.org/10.1029/2019WR026010

Cook, P. G., & Herczeg, A. L. (2000). *Environmental tracers in subsurface hydrology*. Springer Science & Business Media.

Cook, P. G., Love, A. J., Robinson, N. I., & Simmons, C. T. (2005). Groundwater ages in fractured rock aquifers. *Journal of Hydrology*, *308*(1–4), 284–301. https://doi.org/10.1016/j.jhydrol.2004.11.005

Doyle, J., Gleeson, T., Mannning, A., & Mayer, K. (2015). Using noble gas tracers to constrain a groundwater flow model with recharge elevations: A novel approach for mountainous terrain. *Water Resources Research*, *51*, 8094–8113. https://doi.org/10.1002/2015WR017274

Dwivedi, D., Steefel, C. I., Arora, B., Newcomer, M., Moulton, J. D., Dafflon, B., et al. (2018). Geochemical exports to river from the intrameander hyporheic zone under transient hydrologic conditions: East river mountainous watershed, Colorado. *Water Resources Research*, *54*, 8456–8477. https://doi.org/10.1029/2018WR023377

Engdahl, N. B., & Maxwell, R. M. (2015). Quantifying changes in age distributions and the hydrologic balance of a high-mountain watershed from climate induced variations in recharge. *Journal of Hydrology*, *522*, 152–162. https://doi.org/10.1016/j.jhydrol.2014.12.032

Fan, Y., Clark, M., Lawrence, D. M., Swenson, S., Band, L. E., Brantley, S. L., et al. (2019). Hillslope hydrology in global change research and Earth system modeling. *Water Resources Research*, *55*, 1737–1772. https://doi.org/10.1029/2018WR023903

Frisbee, M. D., Phillips, F. M., Campbell, A. R., Liu, F., & Sanchez, S. A. (2011). Streamflow generation in a large, alpine watershed in the southern Rocky Mountains of Colorado: Is streamflow generation simply the aggregation of hillslope runoff responses? *Water Resources Research*, *47*, W06512. https://doi.org/10.1029/2010WR009391

Frisbee, M. D., Wilson, J. L., Gomez-Velez, J. D., Phillips, F. M., & Campbell, A. R. (2013). Are we missing the tail (and the tale) of residence time distributions in watersheds? *Geophysical Research Letters*, *40*, 4633–4637. https://doi.org/10.1002/grl.50895

Gabrielli, C. P., McDonnell, J. J., & Jarvis, W. T. (2012). The role of bedrock groundwater in rainfall-runoff response at hillslope and catchment scales. *Journal of Hydrology*, *450–451*, 117–133. https://doi.org/10.1016/j.jhydrol.2012.05.023

Gabrielli, C. P., Morgenstern, U., Stewart, M. K., & McDonnell, J. J. (2018). Contrasting groundwater and streamflow ages at the Maimai watershed. *Water Resources Research*, *54*, 3937–3957. https://doi.org/10.1029/2017WR021825

Gardner, P. M., & Heilweil, V. M. (2014). A multiple-tracer approach to understanding regional groundwater flow in the Snake Valley area of the eastern Great Basin, USA. *Applied Geochemistry*, *45*, 33–49. https://doi.org/10.1016/j.apgeochem.2014.02.010

Gardner, W. P., Hammond, G. E., & Lichtner, P. C. (2015). High performance simulation of environmental tracers in heterogeneous domains. *Groundwater*, *53*(S1), 71–80. https://doi.org/10.1111/gwat.12148

Gardner, W. P., Hokr, M., Shao, H., Balvin, A., Kunz, H., & Wang, Y. (2016). Investigating the age distribution of fracture discharge using multiple environmental tracers, Bedrichov Tunnel, Czech Republic. *Environmental Earth Sciences*, *75*(20), 1–16. https://doi.org/10.1007/s12665-016-6160-x

Gardner, W. P., Jensco, K. H., Hoylman, Z., Livesay, R., & Maneta, P. M. (2020). A numerical investigation of bedrock groundwater recharge and exfiltration on soil mantled hillslopes. *Hydrological Processes*, *34*(15), 3311–3330. https://doi.org/10.1002/hyp.13799

Gardner, W. P., Susong, D. D., Solomon, D. K., & Heasler, H. P. (2011). A multitracer approach for characterizing interactions between shallow groundwater and the hydrothermal system in the Norris Geyser Basin area, Yellowstone National Park. *Geochemistry, Geophysics, Geosystems*, *12*, Q08005. https://doi.org/10.1029/2010GC003353

Gelman, A., Carlin, J. B., Stern, H. S., Dunson, D. B., Vehtari, A., & Rubin, D. B. (2014). *Bayasien data analysis* (3rd ed.). CRC Press.

Gleeson, T., & Manning, A. H. (2008). Regional groundwater flow in mountainous terrain: Three-dimensional simulations of topographic and hydrogeologic controls. *Water Resources Research*, *44*, W10403. https://doi.org/10.1029/2008WR006848

Hale, C. V., McDonnell, J. J., Stewart, M. K., Solomon, D. K., Doolitte, J., Ice, G. G., & Pack, R. T. (2016). Effect of bedrock permeability on stream base flow mean transit time scaling relationships: 2. Process study of storage and release. *Water Resources Research*, *52*, 1375–1397. https://doi.org/10.1002/2015WR017660

Harmon, R., Barnard, H. R., & Singha, K. (2020). Water table depth and bedrock permeability control magnitude and timing of transpiration-induced Diel fluctuations in groundwater. *Water Resources Research*, *56*, e2019WR025967. https://doi.org/10.1029/2019WR025967

Hayashi, M. (2020). Alpine hydrogeology: The critical role of groundwater in sourcing the headwaters of the world. *Groundwater*, *58*(4), 498–510. https://doi.org/10.1111/gwat.12965

Heaton, T. H. E., & Vogel, J. C. (1981). "Excess air" in groundwater. *Journal of Hydrology*, *50*, 201–216. https://doi.org/10.1016/0022-1694(81)90070-6

Hinsby, K., Højberg, A. L., Engesgaard, P., Jensen, K. H., Larsen, F., Plummer, L. N., & Busenberg, E. (2007). Transport and degradation of chlorofluorocarbons (CFCs) in the pyritic Rabis Creek aquifer, Denmark. *Water Resources Research*, *43*, W10423. https://doi.org/10.1029/2006WR005854

Hubbard, S. S., Williams, K. H., Agarwal, D., Banfield, J., Beller, H., Bouskill, N., et al. (2018). The East River, Colorado, watershed: A mountainous community testbed for improving predictive understanding of multiscale hydrological–biogeochemical dynamics. *Vadose Zone Journal*, *17*(1), 1–25. https://doi.org/10.2136/vzj2018.03.0061

Jung, M., & Aeschbach, W. (2018). A new software tool for the analysis of noble gas data sets from (ground)water. *Environmental Modelling & Software*, *103*, 120–130. https://doi.org/10.1016/j.envsoft.2018.02.004

Kipfer, R., Aeschbach-Hertig, W., Peeters, F., & Stute, M. (2002). Noble gases in lakes and ground waters. *Reviews in Mineralogy and Geochemistry*, *47*(1), 615–700. https://doi.org/10.2138/rmg.2002.47.14

Lerback, J. C., Bowen, B. B., Humphrey, C. E., Fernandez, D. P., Bernau, J. A., Macfarlan, S. J., et al. (2022). Geochemistry and provenance of springs in a Baja California Sur mountain catchment. *Groundwater*, *60*(2), 295–308. https://doi.org/10.1111/gwat.13177

Linde, N., Ginsbourger, D., Irving, J., Nobile, F., & Doucet, A. (2017). On uncertainty quantification in hydrogeology and hydrogeophysics. *Advances in Water Resources*, *110*, 166–181. https://doi.org/10.1016/j.advwatres.2017.10.014

Maloszewski, P., & Zuber, A. (1982). Determining the turnover time of groundwater systems with the aid of environmental tracers 1. Models and their applicability. *Journal of Hydrology*, *57*(3–4), 207–231. https://doi.org/10.1016/0022-1694(82)90147-0

Manning, A. H., Ball, L. B., Wanty, R. B., & Williams, K. H. (2021). Direct observation of the depth of active groundwater circulation in an alpine watershed. *Water Resources Research*, *57*, e2020WR028548. https://doi.org/10.1029/2020WR028548

Manning, A. H., & Caine, J. S. (2007). Groundwater noble gas, age, and temperature signatures in an Alpine watershed: Valuable tools in conceptual model development. *Water Resources Research*, *43*, W04404. https://doi.org/10.1029/2006WR005349

Manning, A. H., Clark, J. F., Diaz, S. H., Rademacher, L. K., Earman, S., & Niel Plummer, L. (2012). Evolution of groundwater age in a mountain watershed over a period of thirteen years. *Journal of Hydrology*, *460–461*, 13–28. https://doi.org/10.1016/j.jhydrol.2012.06.030

Manning, A. H., & Solomon, D. K. (2003). Using noble gases to investigate mountain-front recharge. *Journal of Hydrology*, *275*(3–4), 194–207. https://doi.org/10.1016/S0022-1694(03)00043-X

Marçais, J., Derry, L. A., Guillaumot, L., Aquilina, L., & de Dreuzy, J. R. (2022). Dynamic contributions of stratified groundwater to streams controls seasonal variations of streamwater transit times. *Water Resources Research*, *58*, e2021WR029659. https://doi.org/10.1029/2021WR029659

Markovich, K. H., Condon, L. E., Carroll, K. C., Purtschert, R., & McIntosh, J. C. (2021). A mountain-front recharge component characterization approach combining groundwater age distributions, noble gas thermometry, and fluid and energy transport modeling. *Water Resources Research*, *57*, e2020WR027743. https://doi.org/10.1029/2020WR027743

Markovich, K. H., Manning, A. H., Condon, L. E., & McIntosh, J. C. (2019). Mountain-block recharge: A review of current understanding. *Water Resources Research*, *55*, 8278–8304. https://doi.org/10.1029/2019WR025676

Markovich, K. H., Maxwell, R. M., & Fogg, G. E. (2016). Hydrogeological response to climate change in alpine hillslopes. *Hydrological Processes*, *30*(18), 3126–3138. https://doi.org/10.1002/hyp.10851

Masbruch, M. D., Chapman, D. S., & Solomon, D. K. (2012). Air, ground, and groundwater recharge temperatures in an alpine setting, Brighton Basin, Utah. *Water Resources Research*, *48*, W10530. https://doi.org/10.1029/2012WR012100

Massoudieh, A., Sharifi, S., & Solomon, D. K. (2012). Bayesian evaluation of groundwater age distribution using radioactive tracers and anthropogenic chemicals. *Water Resources Research*, *48*, W09529. https://doi.org/10.1029/2012WR011815

McCallum, J. L., Cook, P. G., Dogramaci, S., Purtschert, R., Simmons, C. T., & Burk, L. (2017). Identifying modern and historic recharge events from tracer-derived groundwater age distributions. *Water Resources Research*, *53*, 1039–1056. https://doi.org/10.1002/2016WR019839

McCallum, J. L., Cook, P. G., & Simmons, C. T. (2015). Limitations of the use of environmental tracers to infer groundwater age. *Groundwater*, *53*(S1), 56–70. https://doi.org/10.1111/gwat.12237

McDonnell, J. J., & Beven, K. (2014). Debates—The future of hydrological sciences: A (common) path forward? A call to action aimed at understanding velocities, celerities and residence time distributions of the headwater hydrograph. *Water Resources Research*, *50*, 5342–5350. https://doi.org/10.1002/2013WR015141

McGuire, K. J., & McDonnell, J. J. (2006). A review and evaluation of catchment transit time modeling. *Journal of Hydrology*, *330*(3–4), 543–563. https://doi.org/10.1016/j.jhydrol.2006.04.020

Meyers, Z. P., Frisbee, M. D., Rademacher, L. K., & Stewart-Maddox, N. S. (2021). Old groundwater buffers the effects of a major drought in groundwater-dependent ecosystems of the eastern Sierra Nevada (CA). *Environmental Research Letters*, *16*(4), 044044. https://doi.org/10.1088/1748-9326/abde5f

Michel, R. L., Jurgens, B. C., & Young, M. B. (2018). Tritium deposition in precipitation in the United States, 1953–2012 (Tech. Rep.). U.S. Geological Scientific Investigations Report 2018-5086.

Miltenberger, A., Uhlemann, S., Mukerji, T., Williams, K., Dafflon, B., Wang, L., & Wainwright, H. (2021). Probabilistic evaluation of geoscientific hypotheses with geophysical data: Application to electrical resistivity imaging of a fractured bedrock zone. *Journal of Geophysical Research: Solid Earth*, *126*, e2021JB021767. https://doi.org/10.1029/2021JB021767

Pliler, R., & Adams, J. A. (1962). The distribution of thorium, uranium, and potassium in the Mancos Shale. *Geochimica et Cosmochimica Acta*, *26*(11), 1115–1135. https://doi.org/10.1016/0016-7037(62)90048-0

Plummer, L. N., Busenberg, E., & Cook, P. G. (2006). *Use of chlorofluorocarbons in hydrology: A guidebook*. International Atomic Energy Agency.

Popp, A. L., Pardo-Alvarez, A., Schilling, O. S., Scheidegger, A., Musy, S., Peel, M., et al. (2021). A framework for untangling transient groundwater mixing and travel times. *Water Resources Research*, *57*, e2020WR028362. https://doi.org/10.1029/2020WR028362

Rajaram, H. (2021). Matrix diffusion as a mechanism contributing to fractal stream chemistry and long-tailed transit time distributions. *Geophysical Research Letters*, *48*, e2021GL094292. https://doi.org/10.1029/2021GL094292

Rapp, G. A., Condon, L. E., & Markovich, K. H. (2020). Sensitivity of simulated mountain block hydrology to subsurface conceptualization. *Water Resources Research*, *56*, e2020WR027714. https://doi.org/10.1029/2020WR027714

Ryken, A. C., Gochis, D., & Maxwell, R. M. (2022). Unravelling groundwater contributions to evapotranspiration and constraining water fluxes in a high-elevation catchment. *Hydrological Processes*, *36*(1), 1–14. https://doi.org/10.1002/hyp.14449

Schilling, O. S., Parajuli, A., Tremblay Otis, C., Müller, T. U., Antolinez Quijano, W., Tremblay, Y., et al. (2021). Quantifying groundwater recharge dynamics and unsaturated zone processes in snow-dominated catchments via on-site dissolved gas analysis. *Water Resources Research*, *57*, e2020WR028479. https://doi.org/10.1029/2020WR028479

Singha, K., & Navarre-Sitchler, A. (2021). The importance of groundwater in critical zone science. *Groundwater*, *60*(1), 27–34. https://doi.org/10.1111/gwat.13143

Singleton, M. J., & Moran, J. E. (2010). Dissolved noble gas and isotopic tracers reveal vulnerability of groundwater in a small, high-elevation catchment to predicted climate changes. *Water Resources Research*, *46*, W00F06. https://doi.org/10.1029/2009WR008718

Solomon, D. K., Hunt, A., & Poreda, R. J. (1996). Source of radiogenic helium 4 in shallow aquifers: Implications for dating young groundwater. *Water Resources Research*, *32*(6), 1805–1813. https://doi.org/10.1029/96WR00600

Solomon, D. K., & Sudicky, E. A. (1991). Tritium and helium 3 isotope ratios for direct estimation of spatial variations in groundwater recharge. *Water Resources Research*, *27*(9), 2309–2319. https://doi.org/10.1029/91WR01446

Somers, L. D., & McKenzie, J. M. (2020). A review of groundwater in high mountain environments. *Wiley Interdisciplinary Reviews: Water*, *7*(6), e1475. https://doi.org/10.1002/wat2.1475

Sprenger, M., Stumpp, C., Weiler, M., Aeschbach, W., Allen, S. T., Benettin, P., et al. (2019). The demographics of water: A review of water ages in the critical zone. *Reviews of Geophysics*, *57*, 800–834. https://doi.org/10.1029/2018RG000633

Stewart, M. K., Morgenstern, U., Gusyev, M. A., & Małoszewski, P. (2017). Aggregation effects on tritium-based mean transit times and young water fractions in spatially heterogeneous catchments and groundwater systems. *Hydrology and Earth System Sciences*, *21*(9), 4615–4627. https://doi.org/10.5194/hess-21-4615-2017

Stute, M., Sonntag, C., Deák, J., & Schlosser, P. (1992). Helium in deep circulating groundwater in the Great Hungarian Plain: Flow dynamics and crustal and mantle helium fluxes. *Geochimica et Cosmochimica Acta*, *56*(5), 2051–2067. https://doi.org/10.1016/0016-7037(92)90329-H

Suckow, A. (2014). The age of groundwater—Definitions, models and why we do not need this term. *Applied Geochemistry*, *50*, 222–230. https://doi.org/10.1016/j.apgeochem.2014.04.016

Tague, C., & Grant, G. E. (2009). Groundwater dynamics mediate low-flow response to global warming in snow-dominated alpine regions. *Water Resources Research*, *45*, W07421. https://doi.org/10.1029/2008WR007179

Tarantola, A. (2005). *Inverse problem theory and methods for model parameter estimation*. SIAM.

Ter Braak, C. J., & Vrugt, J. A. (2008). Differential evolution Markov chain with snooker updater and fewer chains. *Statistics and Computing*, *18*(4), 435–446. https://doi.org/10.1007/s11222-008-9104-9

Thiros, N. E. (2023). Constraining bedrock groundwater residence times in a mountain system with environmental tracer observations and Bayesian uncertainty quantification: Modeling and data package [Dataset]. Zenodo. https://doi.org/10.5281/ZENODO.7554795

Thiros, N. E., Gardner, W. P., & Kuhlman, K. L. (2021). Utilizing environmental tracers to reduce groundwater flow and transport model parameter uncertainties. *Water Resources Research*, *57*, e2020WR028235. https://doi.org/10.1029/2020WR028235

Tokunaga, T. K., Wan, J., Williams, K. H., Brown, W., Henderson, A., Kim, Y., et al. (2019). Depth- and time-resolved distributions of snowmelt-driven hillslope subsurface flow and transport and their contributions to surface waters. *Water Resources Research*, *55*, 9474–9499. https://doi.org/10.1029/2019WR025093

Visser, A., Broers, H. P., Purtschert, R., Sültenfuß, J., & De Jonge, M. (2013). Groundwater age distributions at a public drinking water supply well field derived from multiple age tracers (^{85}Kr, ^{3}H/^{3}He, and ^{39}Ar). *Water Resources Research*, *49*, 7778–7796. https://doi.org/10.1002/2013WR014012

Visser, A., Fourré, E., Barbecot, F., Aquilina, L., Labasque, T., Vergnaud, V., & Esser, B. K. (2014). Intercomparison of tritium and noble gases analyses, ^{3}H/^{3}He ages and derived parameters excess air and recharge temperature. *Applied Geochemistry*, *50*, 130–141. https://doi.org/10.1016/j.apgeochem.2014.03.005

Visser, A., Thaw, M., Deinhart, A., Bibby, R., Safeeq, M., Conklin, M., et al. (2019). Cosmogenic isotopes unravel the hydrochronology and water storage dynamics of the Southern Sierra critical zone water resources research. *Water Resources Research*, *55*, 1429–1450. https://doi.org/10.1029/2018WR023665

Viviroli, D., Dürr, H. H., Messerli, B., Meybeck, M., & Weingartner, R. (2007). Mountains of the world, water towers for humanity: Typology, mapping, and global significance. *Water Resources Research*, *43*, W07447. https://doi.org/10.1029/2006WR005653

von Rohden, C., Kreuzer, A., Chen Zongyu, Z., & Aeschbach-Hertig, W. (2010). Accumulation of natural SF$_6$ in the sedimentary aquifers of the North China Plain as a restriction on groundwater dating. *Isotopes in Environmental and Health Studies*, *46*(3), 279–290. https://doi.org/10.1080/10256016.2010.494771

Wan, J., Tokunaga, T. K., Brown, W., Newman, A. W., Dong, W., Bill, M., et al. (2021). Bedrock weathering contributes to subsurface reactive nitrogen and nitrous oxide emissions. *Nature Geoscience*, *14*(4), 217–224. https://doi.org/10.1038/s41561-021-00717-0

Welch, L. A., & Allen, D. M. (2014). Hydraulic conductivity characteristics in mountains and implications for conceptualizing bedrock groundwater flow. *Hydrogeology Journal*, *22*(5), 1003–1026. https://doi.org/10.1007/s10040-014-1121-5

Zuber, A., Witczak, S., Rózański, K., Śliwka, I., Opoka, M., Mochalski, P., et al. (2005). Groundwater dating with ^{3}H and SF$_6$ in relation to mixing patterns, transport modelling and hydrochemistry. *Hydrological Processes*, *19*(11), 2247–2275. https://doi.org/10.1002/hyp.5669

References From the Supporting Information

Doherty, J., & Welter, D. (2010). A short exploration of structural noise. *Water Resources Research*, *46*, W05525. https://doi.org/10.1029/2009WR008377